M 2023

U.PORTO
FEUP FACULDADE DE ENGENHARIA
UNIVERSIDADE DO PORTO

COMPUTATIONAL FLUID DYNAMICS AND ADDITIVE MANUFACTURING: PARAMETRIC OPTIMIZATION OF PROCESS UNITS

MARTA RAQUEL FERNANDES ALVES DE SOUSA
MASTER THESIS IN CHEMICAL ENGINEERING
PRESENTED TO THE FACULTY OF ENGINEERING
OF THE UNIVERSITY OF PORTO

Master's in Chemical Engineering

Computational Fluid Dynamics and Additive Manufacturing: Parametric Optimization of Process Units

Master dissertation

of

Marta Raquel Fernandes Alves de Sousa

Developed within the course of dissertation

held in

Associate Laboratory in Chemical Engineering

Supervisor: **Prof. José Daniel Araújo**

Joint supervisor: **Prof. Luís Miguel Madeira**

October 2023

Acknowledgment

Firstly, I would like to express my gratitude to my academic supervisor, Prof. José Daniel Araújo, for the indispensable guidance, patience, and valuable inputs throughout the process of completing this work.

To my co-supervisor, Prof. Luís Miguel Madeira, a sincere thank you for the help, clarification of all doubts and exchange of valuable scientific knowledge.

To Doctor Luís Carlos Matos, for the availability to provide me the laboratorial conditions to carry out the work, and endless kindness throughout the process.

To Joana Almeida, for always finding time in a busy schedule to pass along her knowledge with patience and kindness, and for all the help and advice during this project.

I would also like to express my deepest gratitude to my parents and sister, who have always provided me with unconditional support throughout my journey of growing up and becoming the person I am today.

To Afonso, for the unconditional support, through the good times and the challenging moments, for always being by my side and consistently showing me that nothing is impossible, while encouraging me to dream.

To Inês and Joana, for the wonderful friendship since high school and for always having the right words to say during the most challenging times.

Last but not least, to the friends I made in FEUP, for always reminding that I am not alone in this journey, and for making it the most memorable experience I could ever ask for.

Abstract

The chemical industry heavily depends on the optimization of process units. Undoubtedly, Computational Fluid Dynamics (CFD) reveals itself as a powerful tool for fluid flow analysis and for addressing heat and mass transfer challenges; still, it can be combined with design optimization and Additive Manufacturing (AM) for maximizing efficiency.

This work is essentially divided into two parts. The first step was to experimentally validate the results of numerical simulations produced by a commercial CFD package (*ANSYS Fluent*®). The domain used in simulations was printed through AM, specifically using stereolithography (SLA). With this prototype, it was possible to conduct tracer experiments in single-phase flow. Using the laboratorial conditions, these experiments were replicated computationally.

By comparing the two methods, it was possible to verify that the simulation results can replicate the laboratorial situation, although some small disparities were observed. These discrepancies could be mostly solved by improving small parts of the laboratorial protocol (such as the flow rate measurement) and adjusting the value of the tracer mass diffusivity used in the simulations.

The second phase of the work involved an illustrative example of the optimization of geometric parameters to improve the performance of a catalytic reactor. The modelled reactor consists of a geometry with two inlets (through which different compounds are fed), rectangular-shaped obstacles (catalytic surfaces), and one outlet. The methane oxidation reaction was implemented in the simulation program based on kinetic parameters from the literature. The parameters subjected to optimization included the obstacles' dimensions, the distance between inlets and the first obstacles, the distance between inlets and their inclination angle. Subsequently, an objective function/goal was defined: to maximize the methane conversion (limiting reactant). Thus, an automatic optimization tool was applied based on the *ANSYS Workbench* modules, which employed the Adaptive Single Objective method to find an optimal solution.

After analysing the results obtained from the optimization, it was possible to infer that the geometric parameters have a significant influence on the reactor's performance. These parameters highly affect the levels of mixing and dispersion within the studied domain and, consequently, the amount of both reactants that simultaneous reach the catalytic walls.

Keywords: Computational Fluid Dynamics, Additive Manufacturing, Structured Packed Reactors, Optimization

Resumo

A indústria química depende fortemente da otimização de unidades processuais. Indubitavelmente, a Dinâmica de Fluidos Computacional (CFD) tem-se revelado como uma ferramenta poderosa para análise de escoamento e para a resolução de problemas de transferência de massa e de calor; além disso, pode ser combinada com otimização geométrica e Manufatura Aditiva (AM) para maximizar-se a eficiência.

O presente trabalho encontra-se dividido essencialmente em duas partes. O primeiro passo foi validar experimentalmente os resultados das simulações realizadas por um pacote de CFD comercial (*ANSYS Fluent*®). O domínio utilizado nas simulações foi impresso através de AM, mais especificamente pelo método de estereolitografia. Com este protótipo, foi possível realizar experiências de *tracer* (marcador) em escoamento monofásico. Através das condições experimentais, foi possível replicar estas experiências a nível computacional.

Através da comparação entre os dois métodos, foi possível verificar que os resultados das simulações conseguem replicar a situação laboratorial, apesar de apresentarem algumas disparidades. Estas disparidades podem ser resolvidas através da melhoria do protocolo experimental (por exemplo a medição do caudal volumétrico) e através do ajuste do valor da difusividade mássica do *tracer* utilizado nas simulações.

A segunda fase do trabalho envolveu um exemplo ilustrativo da otimização de parâmetros geométricos para melhorar o desempenho de um reator catalítico. O reator simulado consistiu numa geometria composta por duas entradas (nas quais são alimentados compostos diferentes), por obstáculos de formato retangular (superfícies catalíticas), e numa saída. A reação de oxidação do metano foi implementada na simulação utilizando parâmetros cinéticos da literatura. Os parâmetros otimizados foram as dimensões dos obstáculos, as distâncias entre as entradas e os primeiros obstáculos e entre as duas entradas e a inclinação das entradas. Posteriormente, foi definida a função objetivo: maximizar a conversão de metano (reagente limitante). Assim, foi implementada uma ferramenta de otimização automática no módulo do *Workbench* que utilizou o método Adaptativo de Objetivo Único para encontrar a solução ótima.

Após análise dos resultados obtidos pela simulação, foi possível inferir que os parâmetros geométricos têm uma elevada influência no desempenho do reator. Estes parâmetros influenciam fortemente os níveis de mistura e dispersão no domínio estudado e, consequentemente, a quantidade de ambos os reagentes que atingem simultaneamente as superfícies catalíticas.

Palavras-chave: Dinâmica de Fluidos Computacional, Manufatura Aditiva, Reatores de Leito Estruturado, Otimização

Declaration

I hereby declare, under word of honour, that this work is original and that all non-original contributions are indicated, and due reference is given to the author and source.

Marta Raquel Fernandes Alves de Sousa

Porto, 25th of September of 2023

Index

List of Figures

List of Tables

Notation and Glossary

Latin Characters

C	concentration of species *i*	mol·m^{-3}
Co	Courant number	
D	diameter of the inlet	m
D_m	mass diffusivity coefficient	m^2·s^{-1}
E	energy of the system	J
F_i	molar flow rate of species *i*	mol·s^{-1}
$\vec{g}$	gravitational acceleration	m·s^{-2}
h	enthalpy	J
k	rate constant	s^{-1}·m^{-2}
k_t	thermal conductivity	W·m^{-1}·K^{-1}
p	static pressure	Pa
Q	volumetric flow rate	m^3·s^{-1}
Re	Reynolds number	
T	temperature	K
t	time	s
$\overline{t_r}$	mean residence time	s
v	velocity	m·s^{-1}
V	volume	m^3
W	work	J
X	conversion of species *i*	
y_i	mass fraction of species *i*	

Greek Letters

ρ	density of the fluid	kg·m^{-3}
μ	dynamic viscosity	Pa·s
ω	rotational speed of the peristaltic pump	rpm
τ	space time	s
$\bar{\bar{\tau}}$	viscous stress tensor	N·m^{-2}

Indexes

b	bypass
d	dead
in	inlet
out	outlet

Functions

F(t)	Dimensionless concentration function
E(t)	Residence time distribution function

List of Acronyms

2D	Two Dimensional
3D	Three Dimensional

ALICE	Associate Laboratory for Innovation in Chemical Engineering
AM	Additive Manufacturing
ASO	Adaptive Single Objective
ASTM	American Society for Testing and Materials
CAD	Computer Aided Design
CEFT	Transport Phenomena Research Center
CFD	Computational Fluid Dynamics
FEUP	Faculty of Engineering of the University of Porto
LEPABE	Laboratory for Process Engineering, Environment, Biotechnology and Energy
MISQP	Mixed-Integer Sequential Quadratic Programming
MOGA	Multiple Objective Genetic Algorithm
MR	Monolithic Reactor
NLPQL	Non-Linear Programming by Quadratic Lagrangian
PISO	Pressure-Implicit with Splitting of Operators
RP	Rapid Manufacturing
RTD	Residence Time Distribution
SLA	Stereolithography

1 Introduction

1.1 Framing and presentation of the work

At the present time, the chemical industry is directly linked to a massive environmental footprint since it accounts for around one-third of the total energy consumption and CO_2 emissions in the industrial sector (Kiss and Smith, 2020). Consequently, the modelling, design, and optimization of the involved process units have a crucial and growing impact to make the chemical industry more environmental friendly and profitable (Kiss and Smith, 2020).

Among the wide variety of simulation tools available for an engineer, Computational Fluid Dynamics (CFD) presents itself as an indispensable and consensual tool in the area of design and optimization of process units. In a nutshell, a CFD simulation employs digital computers to solve complex models that generate quantitative information on fluid flow and associated phenomena such as heat, mass transfer and reaction (Eslahpazir *et al.*, 2011). These phenomena are at the core of a significant number of chemical engineering processes and are highly reliant on the operating conditions and geometric parameters of the process units. As a result, it is critical that modern computational approaches are capable of accurately predicting the relation between them and provide the best possible solutions for the specificities of each system.

A geometric optimization based on CFD results will provide tailored and efficient solutions, but it can often be at the expense of the geometry complexity that traditional manufacturing tools can't materialize in a non-expensive and time-consuming way. In this area, Additive Manufacturing (AM) allows almost complete freedom when it comes to complex designs, and it is also characterized by an efficient utilization of energy and resources (Leary, 2020).

At the initial stage of the present work, the aim was to validate the CFD solver by comparing its predictions with experimental results obtained in a laboratorial setup. For that purpose, step input tracer experiments were performed on a 3D printed geometry and replicated by CFD simulations. After this validation step, the main objective was to show the potential of CFD-based optimization tools in the design and optimization of process units. For this purpose, single-phase flow with simultaneous surface reaction was simulated in a bi-dimensional domain to infer on the influence of geometric parameters on the reaction efficiency of the studied systems. Lastly, in the optimization part, it was introduced an automatic optimization methodology, based on geometric parameters and a pre-defined objective function that maximizes the products conversion in the outlet stream.

The CFD simulations were carried out in a licensed software, *ANSYS 2021 R2*. This software embodies many tools that allow the pre-processing, processing, post-processing phases, and further optimization.

1.2 Presentation of the Laboratory

The current thesis was developed within the dissertation course of the Master's Degree in Chemical Engineering at FEUP (Faculty of Engineering – University of Porto). The work was conducted in an academic environment and was co-hosted/supervised by members of two research units – CEFT (www.fe.up.pt/ceft) and LEPABE (www.lepabe.fe.up.pt) – that belong to the Associate Laboratory ALICE (Associate Laboratory for Innovation in Chemical Engineering).

CEFT, which in Portuguese stands for Centro de Estudos de Fenómenos de Transporte, is a research unit integrated into the Chemical and Mechanical Engineering Departments of FEUP. Founded in 1996 by four teachers, CEFT is focused on the sub-domain of transport phenomena bridging the main areas of Chemical and Mechanical Engineering. CEFT's dedication lies essentially in fundamental research where it has reached significant success and built excellent quality scientific knowledge, often branching into practical applications.

The research carried out at CEFT is structured into two main topics:

- ENERGY – With an emphasis on cleaner fuels, such as natural gas and biomass, as well as issues related to the carbon problem, and the hydrogen economy. For these issues, optimization, and development of fuel cell technology and systems for hydrogen production and storage are being developed.
- FLUIDS – Addresses several sub-topics that are related and interact with each other: complex fluid, multiphase flows, intelligent fluids, and biofluids. This approach is supported by the high knowledge of researchers from the group, both in appropriate experimental techniques and in advanced computational methods.

LEPABE was created in 1998, as an interdisciplinary group, to operate mainly at the Chemical Engineering Department of FEUP. LEPABE's research is based in 3 pillars – Sustainability and Energy, Processes and Products, Environment and Health – with the mission of developing innovative processes and products to respond effectively to societal challenges, using the basis of chemical and biological engineering to improve the quality of life, in a sustainable and safe way.

1.3 Contribution of the author to the work

The work performed by the author for this dissertation was mainly divided into two phases. The first step was the learning and understanding, in some extent, about the functioning of the

used software, which was a time-consuming process. Therefore, a considerable amount of time in the execution of this dissertation was dedicated to this aspect. The second step consisted in the work itself: creation and 3D Printing of the model, performance of tracer experiments in the laboratory, replication of the experiments in the simulation software, implementation of a surface reaction in the software and implementation of the optimization loop.

1.4 Organization of the dissertation

This dissertation is composed of 6 chapters: Introduction, Context and State of the Art, Materials and Methods, Results and Discussion, Conclusion, and, lastly, the Assessment of the Work Done.

In Chapter 1 - Introduction - the motivation for the work performed is presented, and the main idea is described: the potential of combining CFD-based optimization tools with additive manufacturing technology to enhance the performance of catalytic reactors.

In Chapter 2 - Context and State of the Art - the main methods used, and the theoretical concepts related to the development of this thesis are presented in order to have a better understanding of the obtained results and about the state-of-art on the addressed thematic.

In Chapter 3 - Materials and Methods – the methods employed for the experimental validation of the CFD solver (3D printing of the vessel and the tracer experiments) are explained; still, the main steps to perform the CFD analysis are stated, emphasizing the pre-processing stage, where the model and its computational mesh are generated.

In Chapter 4 - Results and Discussion - an extensive analysis of the obtained results is done.

In Chapter 5 - Conclusions - the main conclusions taken from the present work are stated.

In Chapter 6 - Assessment of the Work Done – an evaluation of the results and work done is performed, adding some suggestions for future works.

2 Context and State of the art

In this chapter, the key concepts that form the foundation of this document are introduced. To facilitate a better understanding of these concepts and their interrelationships, Figure 2.1 exhibits a scheme of the connections between concepts.

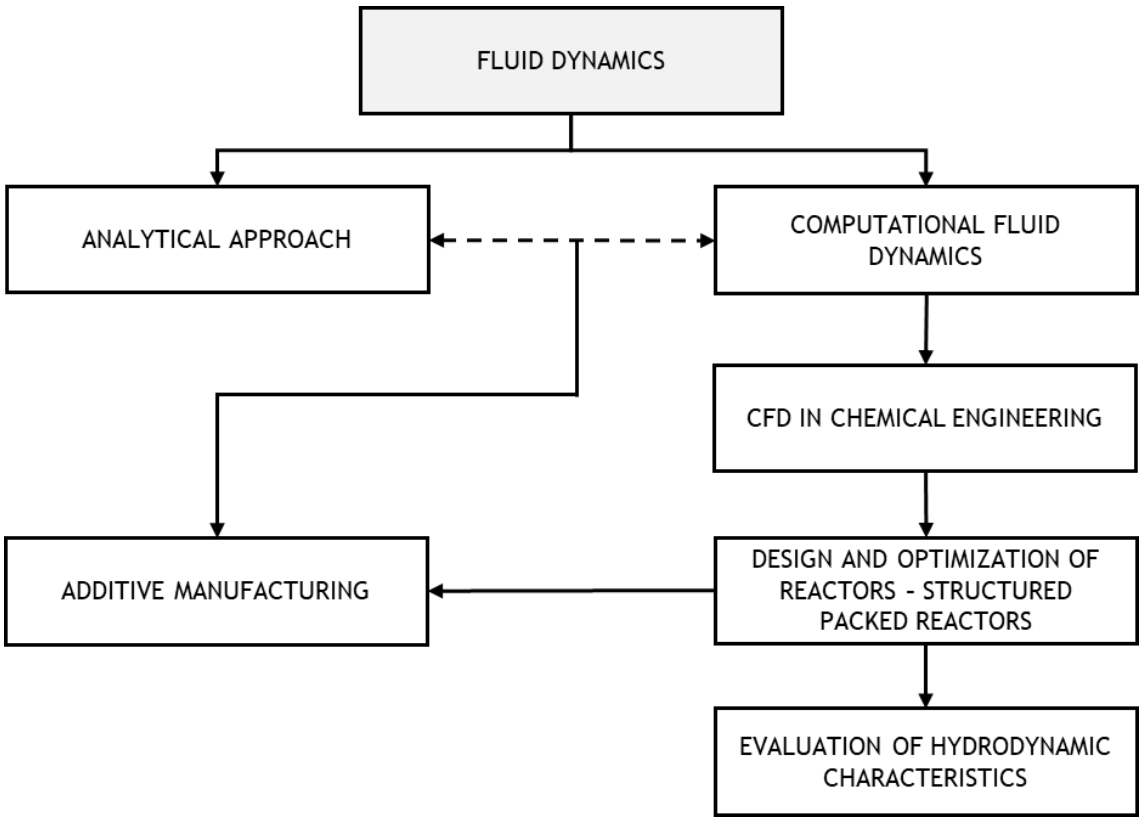

Figure 2.1 Schematic connection between the Context and State of the Art concepts.

Figure 2.1 delineates the key concepts of this work, which is firmly grounded in fluid mechanics. In this project, fluid mechanics is studied into two categories: the traditional approach and the computational approach. The analytical approach is fundamental in the development of foundational principles in fluid mechanics, providing a solid basis for understanding fluid behavior. This approach is the basis of the computational one, in which this work relies on. The computational approach plays a fundamental role in several fields, however, in this work, it will be given notable emphasis on its application in chemical engineering. By employing CFD, it is possible to investigate and assess the hydrodynamic characteristics of process units, that significantly impact the overall performance and efficiency of these units. Additionally, AM plays a dual role in this project. It serves as a critical tool for validating the computational approach by providing physical experimentation data for comparison with CFD results. Furthermore, it exemplifies the wide range of advantages of AM in the chemical industry,

highlighting how this technology can enhance efficiency and innovation in various aspects of chemical engineering.

2.1 Fluid Mechanics

Since the beginning of history to nowadays, mankind has always been intrigued by the movement of fluids, whether it be the water stream in rivers, the wind, the melting of metals, strong ocean currents, or the blood flow within our bodies (Amwel Enterprises, 2008).

The study of fluid mechanics was motivated by necessities such as the creation of water distribution systems for human use and irrigation, the design of ships and boats, and the development of military devices. These advancements were firstly based on the trial-and-error method and did not make use of any mathematical or mechanical principles. The gathering of such empirical knowledge served as a decisive cornerstone for the development that occurred throughout the ancient Greek civilization and, later, the emergence of the Roman Empire. Some of the first texts on fluid mechanics have been found in Archimedes' works, where the ideas of hydrostatics and buoyancy were addressed for the first time (Munson *et al.*, 2005).

The early Renaissance witnessed several contributions that helped to shape what is now known as the foundation of fluid mechanics studies. Many phenomena involving flows were described by Leonardo da Vinci through schematics and writings, while Galileo Galilei's works marked the beginning of experimental mechanics. Many significant contributions were discovered after the early Renaissance period and during the following few centuries (Munson *et al.*, 2005). In the 17th century, Isaac Newton tried to quantify and predict fluid flow phenomena through his elementary Newtonian physical equations. With Newton's work, came many important inputs to fluid mechanics such as Newton's 2nd law and the concept of Newtonian viscosity (Amwel Enterprises, 2008).

In the 18th and 19th centuries, the field of fluid mechanics received an impressive development: Daniel Bernoulli derived the famous Bernoulli equation; Leonard Euler proposed the Euler equations, which describe the conservation of momentum for an inviscid fluid, and the conservation of mass; Claude-Louis Navier and George Gabriel Stokes then introduced viscous transport into the Euler equations, which resulted in the Navier-Stokes equations (Amwel Enterprises, 2008).

2.2 Computational Fluid Dynamics

The Navier-Stokes equations are now the basis of modern-day CFD and are characterized by not having an analytical solution, requiring complex numerical methods. CFD is a field that is supported on fluid mechanics principles and involves numerical approaches and algorithms to simulate, among other aspects, fluid flow around an object (Ahmad and Ayob, 2017). This field

combines the disciplines of fluid mechanics, mathematics, and computer science (Tu *et al.*, 2013).

The first attempt to calculate fluid flow was set forth by Lewis Fry Richardson, with applications for weather forecast. His method required 64 000 men equipped with a calculator to work at the same speed (Suvanjan *et al.*, 2021). Then, with the invention of electric computers, the "human calculators" proposed by Richardson were replaced. Small-scale simulations appeared in literature for the first time in the early 1950s (Suvanjan *et al.*, 2021).

In its early days, CFD was limited to high-technology engineering areas of aeronautics and astronautics, however, nowadays, it is a fundamental tool in many other fields of engineering, such as aerospace, automotive, biomedical, chemical, civil, environmental, and power, among others (Tu *et al.*, 2013). Through CFD, it is possible to gain an increased knowledge of how system components are expected to perform and to make the required improvements for design and optimization studies.

For example, the solution of a scenario with simultaneous fluid dynamics and heat transfer can be achieved by three basic methods: experimental fluid dynamics, analytical fluid dynamics, and CFD. These three approaches are strongly interlinked with each other and do not lie in isolation. The traditional approach to address fluid dynamics and to assist the design of equipment and industrial processes combines analytical and experimental methods. However, with the evolution of technology, CFD has emerged as one indispensable tool. Even though the analytical method is still used by many, the trend is towards greater reliance on the computational approach for industrial designs, particularly when the fluid flows are complex.

2.3 Governing Equations

The term CFD is used to describe a broad range of numerical techniques used for solving complex and time-dependent flow problems (Rapp, 2017). These flow problems embody the three principles of any fluid flow: conservation of mass, energy, and momentum.

For brevity reasons, in this chapter, the meaning of each variable is explained in further detail in the Notation and Glossary section.

2.3.1 Mass Conservation

The mass conservation law lies in the principle that the mass of the fluid flow is immutable, it may neither be created nor destroyed (Anderson, 1995). This law can be well represented by the following equation:

$$\frac{D\rho}{Dt} = 0 \tag{2.1}$$

The parcel $^{D\rho}/_{Dt}$ represents the time rate of change of density of a given fluid element as it moves through space. It can be also represented by the sum of, $^{\partial\rho}/_{\partial t}$, which represents the time rate of change at a fixed point, and $\rho\nabla\cdot\vec{v}$, that physically represents the time rate of change due to the movement of the fluid element from one location to another in the flow field where the flow properties are spatially different. This gives the equation that illustrates the mass conservation law, the continuity equation:

$$\frac{D\rho}{Dt} = \frac{\partial\rho}{\partial t} + \rho\nabla\cdot\vec{v} = 0 \tag{2.2}$$

2.3.2 Momentum Conservation

The momentum equation expresses the law of conservation of momentum for a moving fluid. The rate of the total momentum of any unit in the flow field is equal to the resultant force of all external forces acting on the unit (Aziz, 2010).

The momentum conservation can be referred to as the Navier-Stokes Equation, given by (SimScale, 2023):

$$\overbrace{\frac{\partial}{\partial t}(\rho\,\vec{v})}^{I} + \overbrace{\nabla\cdot(\rho\,\vec{v}\vec{v})}^{II} = \overbrace{-\nabla p}^{III} + \overbrace{\nabla\cdot(\bar{\bar{\tau}})}^{IV} + \overbrace{\rho\vec{g}}^{V} \tag{2.3}$$

Each parcel of the equation has a different denotation: I – local change with time; II – momentum convection; III – surface force; IV – diffusion term; V – mass force.

2.3.3 Energy Conservation

The energy conservation equation results from the application of Thermodynamics 1st Law to an infinitesimal volume of fluid. The energy conservation law states that the energy change is equal to the sum of heat and work by external force in the fluid control volume (Migliorini *et al.*, 2014).

$$dE_t = dQ + dW \tag{2.4}$$

One of the common types of the energy equation is (SimScale, 2023):

$$\rho\left[\overbrace{\frac{\partial h}{\partial t}}^{I} + \overbrace{\nabla\cdot(h\vec{v})}^{II}\right] = \overbrace{-\frac{\partial p}{\partial t}}^{III} + \overbrace{\nabla\cdot(k_t\nabla T)}^{IV} + \overbrace{\phi}^{V} \tag{2.5}$$

Each parcel has the following meaning: I – local change with time; II – convective term; III – pressure work; IV – heat flux; V – source term.

2.4 CFD in Chemical Engineering

Chemical engineering is a field with a wide range of applications. A chemical engineer is able to design, construct, and run machinery for large-scale industrial chemical, biological or related operations. CFD is widely applied in the chemical industry to analyze and optimize the design of chemical processes, such as reactors, distillation columns, and heat exchangers, just to give a few examples. This promising technology can also be applied to analyze the environmental impact of chemical processes, such as the release of pollutants into the atmosphere, air pollution, ventilation, and combustion pollutants prediction.

Chemical engineering and process industries have benefited from the use of CFD by reducing the cost of product and process development and optimization activities, shortening time to market, improving design reliability, and increasing conversions and yields (Mr CFD, 2023).

2.5 Structured packed reactors

Fixed bed and slurry reactors serve as the backbone of the chemical industry, offering the advantages of straightforward construction on one hand, but presenting challenges in terms of unpredictable and turbulent fluid dynamics on the other. Stating this, structured packed reactors assume a pivotal role in the upcoming future (Moulijn and Kapteijn, 2013).

A structured reactor embodies a structured internal component, which can be composed of ceramics, metals, or carbon, positioned within the reactor itself. A monolith is the most well-known type of structured packed reactor (Pangarkar *et al.*, 2008).

The name “monolith” stems from the Greek *mono* and *lithos*, single and stone. In catalytic reaction engineering, a monolith is defined as a single block of catalyst-containing material through which reactants and products are transported by convection (Moulijn and Kapteijn, 2013).

A monolithic reactor (MR) is composed of a large number of parallel channels, the monoliths, all of which containing catalyst coat on their inner walls. MRs offer structured, well-defined flow paths for the reactive flow, making the residence time of the reaction flow predictable (Önsan and Avci, 2016). Monoliths have been applied in several chemical processes but are mainly known for their use in the automotive industry (Lopes and Rodrigues, 2016). In Figure 2.2, a scheme of a monolith and a MR are represented.

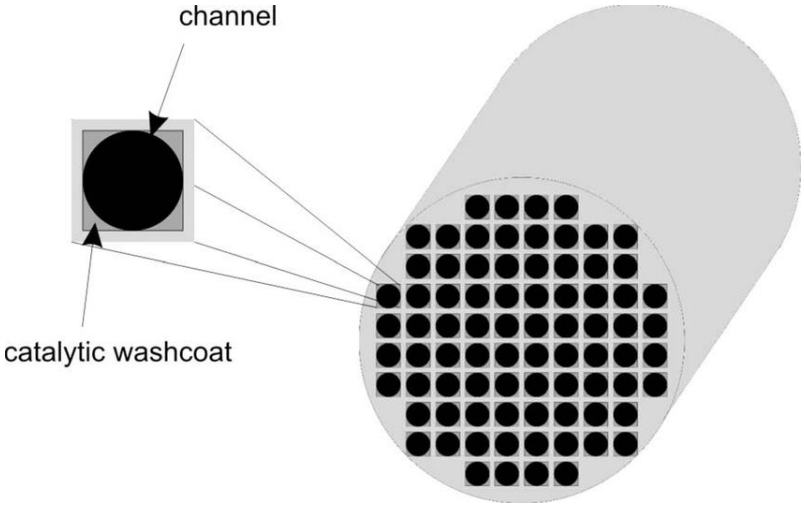

Figure 2.2. MR scheme; taken from: Raberger et al. (2009).

The wall thickness and its characteristic dimension present themselves as independent variables since they influence different parameters. The wall thickness determines the molecular transport rate, and the channel size the pressure drop. The freedom introduced by monoliths' ability to let users select the length scales on their own opens up possibilities for the highest possible catalyst performance with the lowest pressure drop (Kreutzer *et al.*, 2006).

Heat management in MRs via external heating or cooling is not very effective due to the lack of convective heat transport in the radial direction. The material of construction of the monolithic structure affects the overall performance. MRs can be made of metal, in the case of nonadiabatic reactions, since metal has a higher thermal conductivity and partially eliminates the lacking convective contribution, or ceramics, for adiabatic reactions (Önsan and Avci, 2016).

Overall, MRs offer many advantages when compared to other types of reactors, such as low pressure drops, and the elimination of resistances to heat and mass transfer; they show low axial dispersion, and a high surface area (Lopes and Rodrigues, 2016).

Structured internals often come with certain drawbacks, such as limited catalyst loading, especially when the catalyst is applied as a coating, and elevated expenses. To attain catalyst loadings comparable to those in randomly packed beds, it is essential to have either a substantial geometric surface area for the structured internals or incorporate an integrated structured catalyst (Pangarkar *et al.*, 2008).

A thorough understanding of hydrodynamics and transport parameters is crucial for the effective design of structured catalytic reactors. CFD emerges as a crucial tool in achieving this understanding (Pangarkar *et al.*, 2008). By employing CFD simulations it is possible to model and analyze the patterns of fluid flow, enabling detailed examination of how reactants and products behave through the reactor.

2.6 Hydrodynamic Characteristics

In order to predict the behavior of a process unit, the hydrodynamic characterization of the flow acquires great importance.

First of all, it is relevant to mention one of the most important dimensionless groups in fluid mechanics – the Reynolds number. This dimensionless group represents the ratio between inertial forces and viscous forces. This number is used to classify fluid systems where viscosity plays a significant role in regulating fluid velocities and flow patterns. The Reynolds number is defined as (Rehm *et al.*, 2008):

$$\mathrm{Re} = \frac{\text{inertial forces}}{\text{viscous forces}} = \frac{\rho v D}{\mu} \tag{2.6}$$

This number is used to determine whether a fluid is in laminar or turbulent flow. For a single-phase flow in a pipe, if the Reynolds number is lower than 2100, the viscous forces overlap the inertial forces, so the flow is classified as laminar. On the other hand, if the Reynolds number is higher than 4000, the inertial forces are dominant and the flow is turbulent (Campos, 2013).

2.6.1 Residence Time Distribution

The determination of the residence time distribution (RTD) function is an effective method that extracts relevant information about the flow pattern in a vessel. This distribution function can be estimated by tracer studies. In these studies, a tracer, which is an inert species, is injected into the system and by measuring the its outlet concentration, it is possible to get an important insight about the flow in the reactor (or any other device) (Fogler, 1999).

The Danckwerts' *F* curve represents the ratio between the tracer concentration at the outlet of the reactor and the concentration of the injected tracer for a step change at the inlet, and it can be easily interpreted as the average dimensionless concentration evolution at the outlet (Danckwerts, 1953):

$$F(t) = \frac{C_{out}(t)}{C_{in}} \tag{2.7}$$

where C_{out} is the average tracer concentration at the outlet, and C_{in} is the average tracer concentration at the inlet during the step change.

With the F(t) curve, the RTD function, E(t), can be obtained by doing the derivative of the F(t) function:

$$F(t) = \int_0^t E(t)dt \;\Leftrightarrow E(t) = \frac{dF(t)}{dt} \tag{2.8}$$

This function (particularly the product $E(t) \cdot dt$) quantifies the fraction of fluid elements with residence time between t and $t + dt$. From the E(t) distribution function, it is possible to calculate the mean residence time, $\bar{t_r}$, defined as:

$$\bar{t_r} = \int_0^\infty tE(t)dt \tag{2.9}$$

This equation can be interpreted as the calculation of the area below the $t \cdot E(t)$ function.

The comparison between the value of the mean residence time calculation and the space-time, τ (given by the ratio between the reactor volume, V, and the total flow rate, Q – cf. Eq. 2.10), provides an important information about the reactor performance.

$$\tau = \frac{V}{Q} \tag{2.10}$$

If $\bar{t_r} > \tau$, there is a short-circuit in the flow (bypass) or the presence of preferential paths, on the other hand, if $\bar{t_r} < \tau$, then there are dead or stagnant zones inside the vessel.

In case there is a stagnant region, the dead volume fraction, ${V_d}/{V}$, is determined by:

$$\frac{V_d}{V} = 1 - \frac{\bar{t_r}}{\tau} \tag{2.11}$$

Analogously, the bypass flow rate fraction, ${Q_b}/{Q}$, is determined by:

$$\frac{Q_b}{Q} = 1 - \frac{\bar{t_r}}{\tau} \tag{2.12}$$

2.6.2 Conversion

Since the main focus of this work is to optimize the geometry of a structured packed reactor, it is important to assess the conversion of a reaction. The conversion of an i component, X_i, is defined as:

$$X_i = \frac{F_{i0} - F_i}{F_{i0}} \tag{2.13}$$

where F_{i0} represents the molar flow rate of species i that is fed to the reactor, and F_i the molar flow rate of such species at the outlet (Constales *et al.*, 2017).

If the volumetric flow rates are constant, the conversion can also be calculated as:

$$X_i = \frac{C_{i0} - C_i}{C_{i0}} \tag{2.14}$$

where C_{i0} represents the concentration of species i that is fed to the reactor, and C_i its concentration at the outlet (Constales *et al.*, 2017).

2.7 Additive Manufacturing

Additive Manufacturing (AM), also known as 3D printing, is defined by the American Society for Testing and Materials (ASTM) as a "process of joining materials to make objects from 3D model data, usually layer upon layer, as opposed to subtractive manufacturing methodologies" (ASTM, 2009). In other words, AM is a family of techniques that enables the fabrication of a solid object from a computer-aided design (CAD) (Capel *et al.*, 2018).

In the 1980s, additive manufacturing was first used to develop prototypes, however, these objects were not usually functional. This process was known as Rapid Prototyping (RP) because it allowed the creation of a scale model of the final product in a fast manner and without the usual setup time and the expense associated with producing a prototype. As AM evolved, its applications expanded to rapid tooling, which was used to create molds for the final products (Kumar and Prasad, 2021).

Similar to RP, AM involves the production of parts layer-by-layer. In AM technology, to form a layer, the material is deposited on the previous layer and fused to it by the application of energy such as thermal, chemical, or mechanical. The AM technology offers several advantages over conventional manufacturing methods, such as reduced production costs, the possibility of fabrication of high complexity components, the wide range of materials that can be used, and provides a lower waste and material costs (Leary, 2020). In terms of industrial machinery, assembly procedures, and supply chains, AM technologies have the potential to drastically alter conventional production patterns (Gao *et al.*, 2015).

AM embodies many methods, which can be utilized according to the final application of the prototype. These methods include fused deposition modelling, powder bed fusion, inkjet printing and contour crafting, stereolithography, direct energy deposition, and laminated object manufacturing (Ngo *et al.*, 2018).

The available devices in the laboratory allow using a commercial 3D printer by Upside-Down Stereolithography (SLA) *(FormLabs*®). SLA is one of the earliest methods of additive manufacturing, which was developed in 1986 (Ngo *et al.*, 2018) and is a layer-by-layer structure-building technology (Catarino *et al.*, 2017). A scheme of the upside-down SLA is represented in Figure 2.3.

Figure 2.3. 3D printer scheme by Upside-Down SLA scheme; taken from: (FormLabs, 2023).

As it is possible to observe, a laser beam is focused on the free surface of a photosensitive liquid, in this case resin, to induce polymerization and change the liquid into a polymerized solid (FormLabs, 2023).

SLA provides a final piece with fine resolution and high quality and has a highly versatile material selection. On the other hand, the speed of printing is highly dependent on the moving laser beam due to the curing rate (Quan *et al.*, 2020). Overall, SLA is a valuable tool used in a wide range of industries such as engineering, product design, dentistry, jewellery, model making and education (FormLabs, 2023).

2.7.1 3D Printing in Chemical Engineering

The idea of process intensification, which strives to create chemical products more sustainably and efficiently, is frequently linked to current advancements in chemical engineering. One area of study is the use of novel approaches in equipment design to increase process efficiency. For example, continuous flow reactors that use heterogeneous catalysts are currently constrained by mass, momentum, or energy transfer and provide the best prospects for process intensification using AM (Parra-Cabrera *et al.*, 2018).

In this regard, with the course of time AM has progressively evolved into a commonplace instrument within the daily routines of chemical engineers, particularly within the domains of research, development, and optimization (Amores *et al.*, 2022).

AM offers a multitude of exciting possibilities in many respects, being two of them the ability to create complex shapes that are difficult to achieve using other manufacturing techniques and the ability to do so on a small scale, as opposed to other methods that require the production of large-scale quantities of the same products to be worthwhile. This technology enables the production of reactors, mixing devices, and packed columns with improved geometries for continuous flow and batch operations. It also allows the production of filters, adsorbent structures, and membranes. In this sense, 3D Printing can help to develop more sustainable chemical production systems (Amores *et al.*, 2022).

3 Materials and Methods

3.1 Validation of the CFD solver

The validation step of the CFD simulation tool (*ANSYS Fluent*®) consisted in conducting tracer experiments on a laboratory scale vessel and the replication of these experiments by simulation in the *ANSYS* software. The laboratorial stage can be divided into two main parts: 1) the 3D design and printing of an illustrative vessel filled with obstacles; 2) the execution of tracer experiments based on a step input at the inlet.

3.1.1 3D Printing

The first step was to create a 3D vessel using a CAD software, specifically *SOLIDWORKS*®. The geometry of the flow domain included rectangular obstacles, and their orientations varied between horizontal and vertical within the overall flow domain. The model was designed to incorporate two conical adaptors at the inlet and outlet, allowing for a seamless connection between the existing laboratory tubes and the printed component. By utilizing *SOLIDWORKS*®, the necessary geometrical features and specifications were incorporated into the 3D design, ensuring its compatibility with the subsequent printing process. The created vessel and its dimensions, in mm, can be visualized in Figure 3.1.

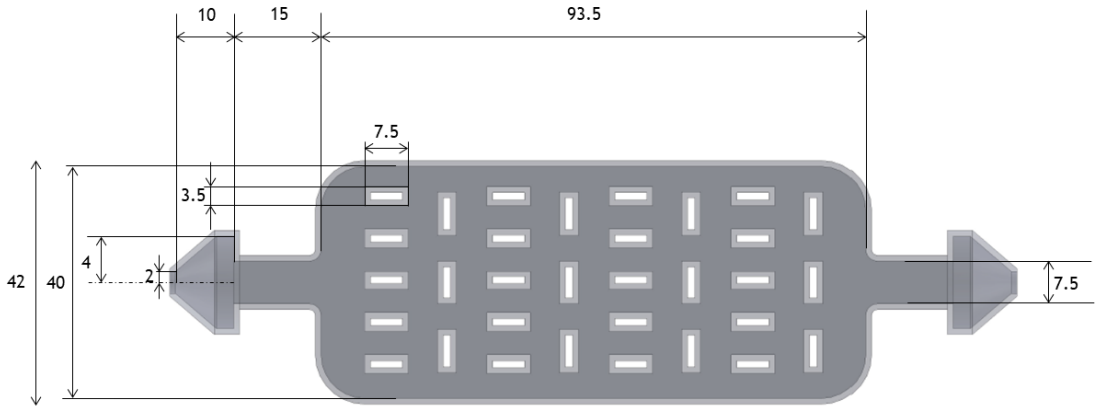

Figure 3.1. Geometry created in SOLIDWORKS® and its dimensions in mm.

The 2D sketch of the geometry was extruded with a depth of 10 mm, and a shell thickness of 1 mm was created in the outward direction, resulting in a hollow structure. Figure 3.2 illustrates an isometric view of the 3D vessel.

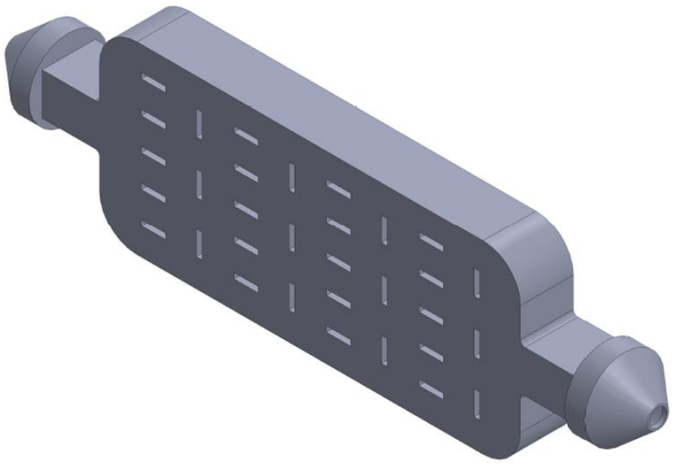

Figure 3.2. Isometric view of the 3D Model created in SOLIDWORKS®.

Once the 3D vessel was created and exported in a .stl file, it was imported into the printing software, *PreForm*®. Here, the software detected some instability in the original design, which required the introduction of supports in the basis and sides of the vessel. These supports took the form of mini rafts, featuring a touch point size of 0.45 mm and a height of 5 mm. This ensured stability and prevented deformation during the printing process. After the quality of printing was ensured, an adaptive layer thickness was chosen, allowing the software to determine the appropriate layer thickness for each section of the printing. Considering the chosen settings, an estimation of the printing time was 2 h 50 min for a total of 334 layers. Figure 3.3 depicts the printing preview given by the program.

Figure 3.3. 3D Printing preview with the supports.

The piece above was printed with a clear resin in order to allow the visualization of the inside of the vessel. Following the completion of the printing process, the printed piece was rinsed in isopropyl alcohol. This step is crucial to remove any residual or uncured resin from the surface of the printed component. Subsequently, the piece underwent a curing process, where it was exposed to ultraviolet light during 15 minutes at 60°C.

3.1.2 Experimental Setup and Procedure

The RTD experiments involved the use of water as the base fluid along with an inert tracer. In this case, indigo carmine was selected as the tracer due to its blue color, which facilitated visualizing the flow evolution. The experimental procedure commenced by filling the printed piece with water using a peristaltic pump. During this process, the spectrophotometer was calibrated to register a value of zero absorbance when water passed though the measurement cell. Subsequently, the injection of the aqueous tracer solution commenced, and the absorbance at the outlet of the vessel was continuously recorded at a wavelength of 588 nm. The recording process ceased once the absorbance reached a stable value, indicating a tracer concentration at the outlet similar to the one at the inlet (*F* curve, i.e., dimensionless outlet concentration of nearly 1).

Throughout the experimental tests, the flowrate was measured at various intervals using a beaker and a stopwatch. Additionally, it was necessary to measure the delay caused by the fluid in the tubing (from the reservoir to the inlet of the vessel and from the outlet to the spectrophotometer's cell) to subtract to the experimental data at each flow rate tested.

Figure 3.4 illustrates the schematic representation of the experimental setup, while Figure 3.5 depicts the physical setup employed in the laboratory for conducting these tracer experiments.

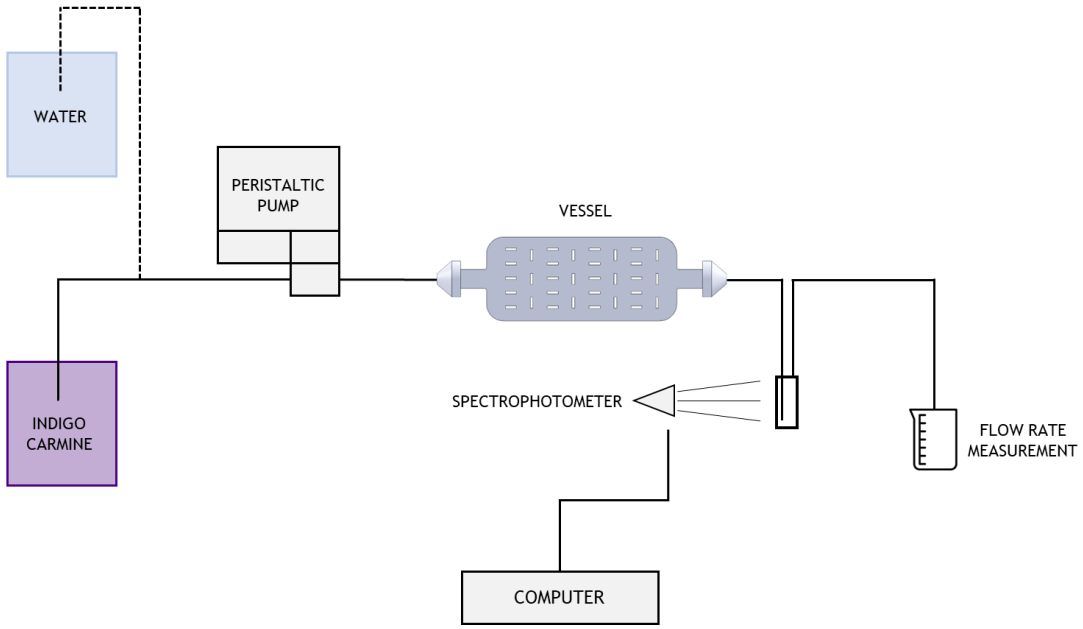

Figure 3.4. Experimental setup scheme for the tracer experiments.

Figure 3.5. Photo of the experimental setup in the laboratory.

3.1.3 Tracer Experiments Simulation

The CFD approach consists in 3 major steps: pre-processing, processing, and post processing. The pre-processing stage involves the creation of the geometry and the generation of its computational mesh. This part was carried out in *Workbench*, a software platform that integrates various *ANSYS* products and enables seamless connection between them, as shown in Figure 3.6.

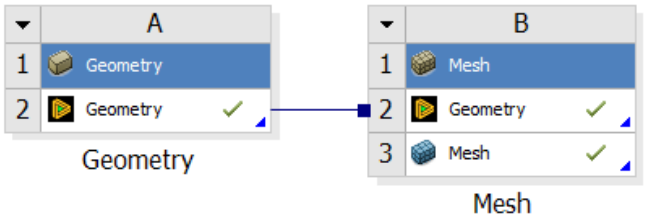

Figure 3.6. Pre-Processing in Workbench.

In the pre-processing stage of the CFD approach, the geometry was initially created using *DesignModeler*, a module within the *ANSYS* software suite. The dimensions of the created geometry, expressed in mm, are provided in Figure 3.7.

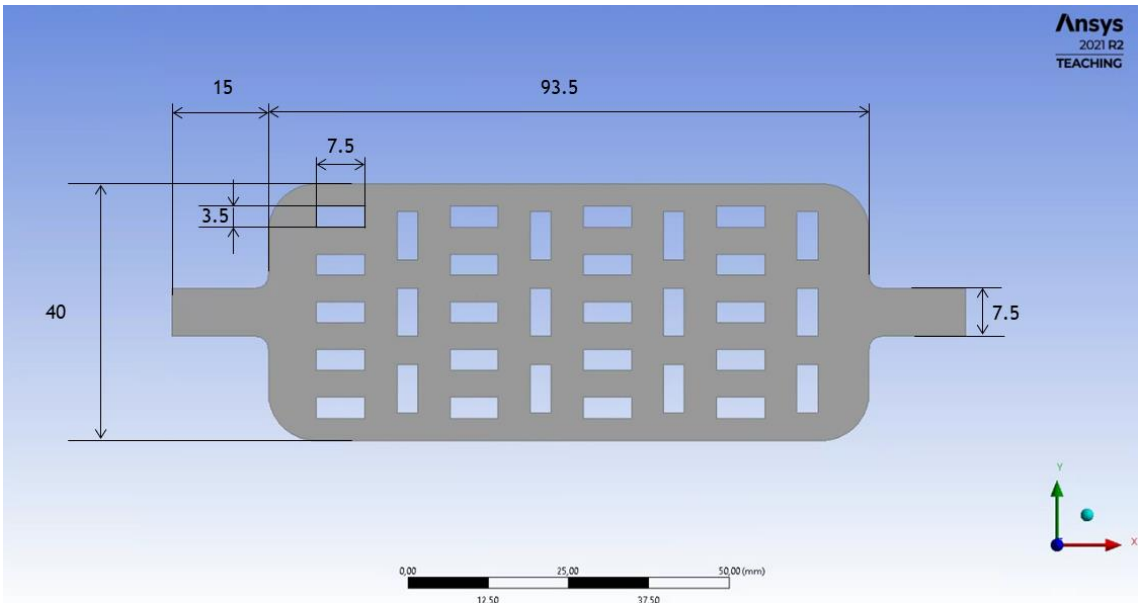

Figure 3.7. Geometry in DesignModeler and its dimensions in mm.

For the simulations, a 2D domain of the 3D printed vessel was employed. However, to maintain a certain level of accuracy in the obtained results, a modification was made to the depth, setting it to 10 mm in the *Reference Values* command within the *Fluent* software. By implementing this approach, the computational time was reduced without compromising the essential aspects of the flow's behavior under analysis.

In the second step of the pre-processing stage, carried out on the *Meshing* module, the focus is on generating the computational mesh. This involves dividing the mathematical domain into smaller elements, where the model equations will be solved during the simulation. The size of these elements, known as the element size, has an impact on both the computational time required for the simulations and the quality of the results obtained. In this case, the computational mesh was generated with elements of 0.4 mm size. This size was chosen based on mesh independence tests (Appendix A).

During the meshing process, the boundaries of the computational domain were also defined: the inlet, the outlet, and the walls of the flow domain. These boundary conditions are essential for setting up the simulation. Figure 3.8 illustrates the representation of the generated computational mesh.

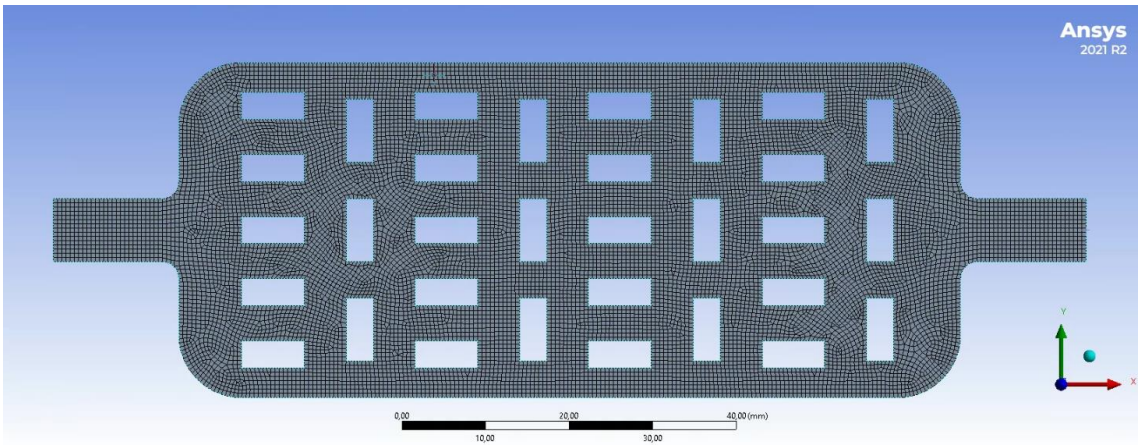

Figure 3.8. Computational mesh for the tracer experiments.

After completing the geometry and meshing process, the subsequent step was carried out in *Fluent*, where the simulation itself took place. In *Fluent*, the simulation setup involved defining the boundary conditions, fluid properties and selecting the appropriate calculation methods. In this case, all simulations were performed in the transient state, capturing time dependent flow behavior.

The first step in the setup was choosing the models. For the flow, a *Viscous-Laminar* model was selected, as the simulations were conducted at low Reynolds numbers. Additionally, the *Species Transport* model was activated to allow for the simulation of a flow mixture comprising different species.

Following the model selection, the materials for the simulation were created. Water and the aqueous tracer solution were defined as separate materials but with the same properties (the tracer should not affect the hydrodynamics and have properties as close as possible to the fluid, which was the case). The mixture of these two species was also defined. As the energy equation was not included in this case, i.e., it was assumed isothermal experiments, the density of the mixture was determined using a *Volume-Weighted Mixing Law*, while the viscosity was determined using a *Mass-Weighted Mixing Law*.

Furthermore, the simulation setup required defining the mass diffusivity, D_m, of the tracer in the mixture. For this purpose, a standard value of 1×10^{-9} $m^2 \cdot s^{-1}$ was assigned, which represents a typical value for mass diffusivity between two liquids. The properties of the fluids used in the simulation are presented in Table 3.1.

Table 3.1. Physical properties of the materials defined in Fluent.

ρ / kg·m^{-3}	μ / Pa·s	D_m / m^2·s^{-1}
998.2	0.001	1×10^{-9}

After creating the materials and defining their properties, the next step in the simulation setup was to establish the boundary conditions. In this case, the condition of particular interest was the velocity of the flow at the inlet, where the tracer solution enters the domain. This velocity was determined based on the volumetric flow rate values obtained from the laboratory experiments.

With the simulation setup completed and the boundary conditions defined, it was time to proceed to the solution phase. This involved choosing solution methods and defining convergence criteria. The convergence criteria are typically specified by setting a target value for the Residuals, which quantify the allowed error in the solution of the system equations. A lower residual value indicates more accurate results, but more time-consuming. In these simulations, the *Residuals* were defined as 1×10^{-5}.

As the tracer simulations were performed in the transient state, the selected solution method was *PISO* (Pressure-Implicit with Splitting of Operators). This method is commonly used for transient simulations and offers reliable and accurate results.

During the initialization task, the mass fraction of water inside the domain was set to 1, representing the initial condition of the domain being filled with pure water. Additionally, the number of time steps and the time step size had to be defined. In this case, the adaptive feature was chosen, allowing the software to automatically determine the most suitable size for each time step. In this step, the Courant number (Co) also had to be defined. This number quantifies how much information propagates across a computational grid cell in a given unit of time and it should not exceed 1. If it exceeds 1, it can lead to inaccuracies in the solution (IdealSimulations, 2020). At this point, the Co was set to 1 since it was assumed to be appropriate for the case.

3.2 Direct Optimization

After ensuring that the chosen method provides reliable results, the subsequent step involves the geometric optimization of a vessel filled with catalytic walls considering an illustrative (model) reaction. In this phase, the principal aim is to employ a parametric optimization of the reactor's geometric configuration with the objective of enhancing the reactor performance, specifically by maximizing the conversion of the limiting reactant.

The performance of this component embodied several steps: the creation of the reactor's geometry in *DesignModeler*, including the specification of the geometric parameters, the generation of the computational mesh in *Meshing*, the establishment of the chemical reaction and its kinetics within *Fluent*, and the utilization of the direct optimization feature available in *Workbench*.

3.2.1 Geometry and Mesh Generation

The geometry comprised a vessel with two inlets, the presence of rectangular obstacles representing the catalytic surfaces, and an outlet. Figure 3.9 exhibits the created geometry, along with its dimensions, in mm, and optimization parameters.

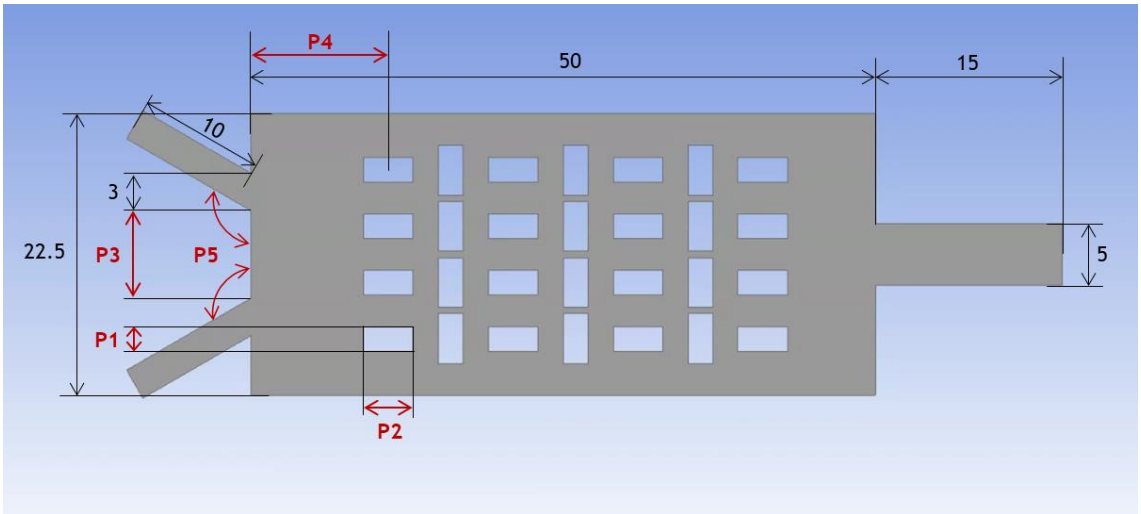

Figure 3.9. Geometry of the reactor along with the dimensions, in mm, and geometric parameters to be optimized (red arrows).

As it is possible to see in Figure 3.9, the selected parameters to be optimized were the dimensions of the obstacles (P1 and P2), the distance between inlets (P3), the distance between the inlets and the first obstacles (P4), and the angle between the inlet and the vertical axis (P5).

After the creation of the geometry, the computational mesh was generated employing an element size of 0.2 mm. The selection of this specific size was chosen upon the results of mesh independence tests (Appendix A). In this step, the boundaries were also created: the two inlets for both reactants ("inlet_A" and "Inlet_B"), the outlet ("outlet"), the external walls of the reactor ("walls") and the catalytic walls of the obstacles where the reaction shall take place ("walls_react").

3.2.2 Simulation Setup

The main objective of this stage was to implement an illustrative wall surface reaction in the simulation system. Therefore, the chosen reaction was the oxidation of methane:

$$CH_4 + 2O_2 \rightarrow CO_2 + 2H_2O \tag{2.15}$$

The kinetic equation and parameters were based in literature values for this reaction with a nickel catalyst at 928 K (Aryafar and Zaera, 1997):

$$r = kP_{CH_4}^{0.9} P_{O_2}^{0.2} \tag{2.16}$$

where k represents the rate constant and can be calculated with the Arrhenius equation:

$$k = 1.3 \times 10^{6} e^{-\frac{1.18\times10^{5}}{RT}} \tag{2.17}$$

It is important to highlight that the energy equation was not considered in these simulations, as the primary focus of this study centers on the mass domain. The investigation of heat transfer can be taken for a more comprehensive analysis in future works.

In *Fluent*, the first step was to define the simulation models. Firstly, the *Viscous-Laminar* and the *Species-Transport* models were activated and within the *Species-Transport* activation, the reaction was activated by selecting the *Volumetric* and *Surface Reaction* options.

The next step was to create the species: CH_4, O_2, CO_2, H_2O, and N_2 (inert species), which were retrieved from the *Fluent* database along with their properties.

Following the creation of the species, the next step involved the definition of the reaction as a *Wall Surface* type, i.e., the reaction only occurs in the regions defined as walls (catalytic surfaces), the definition of the stoichiometry, and the kinetic parameters.

The mixture of these species was also defined, setting the density of the mixture as *Volume-Weighted Mixing Law*, and the viscosity as a *Mass-Weighted Mixing Law*. The value of the mass diffusivity was set by default in *Fluent* with a value of 2.88×10^{-5} $m^2 \cdot s^{-1}$.

Following this, the boundary conditions were defined. The walls of the obstacles were characterized as the catalytic surface where the designated chemical reaction occurred. During this stage, the software provided the option to specify certain catalytic parameters, such as reaction mechanism. However, this aspect was not explored in the present work and as such the default values provided by the software were employed.

In both inlets, the velocity was defined as 0.4 $m \cdot s^{-1}$. According to literature, the feeding of the reactor should have O_2 in excess, CH_4 and N_2. Table 3.2 contains the composition of both feeds.

Table 3.2. Composition of both inlets.

	CH_4	**O_2**	**N_2**
Inlet A	-	0.900	0.100
Inlet B	0.135	-	0.865

The chosen calculation method was *Coupled*, which is reliable for steady state flow simulations. The *Residuals* were defined as 1×10^{-5}, the simulation was initialized with the reactor filled with N_2, and the calculations were made until reaching convergence.

Subsequently, it was necessary to establish an output parameter, in this case the conversion of CH_4, to use in the further optimization loop. To achieve this, a *Named Expression* was created

(within the software) as the ratio between the average molar concentration of CO_2 at the outlet and the average molar concentration of CH_4 at inlet B.

3.2.3 Optimization Loop

For the optimization step, a fully automatic iterative optimization methodology was employed by choosing the *Direct Optimization* feature in *Workbench* and connecting it to the setup previously made, as shown in Figure 3.10.

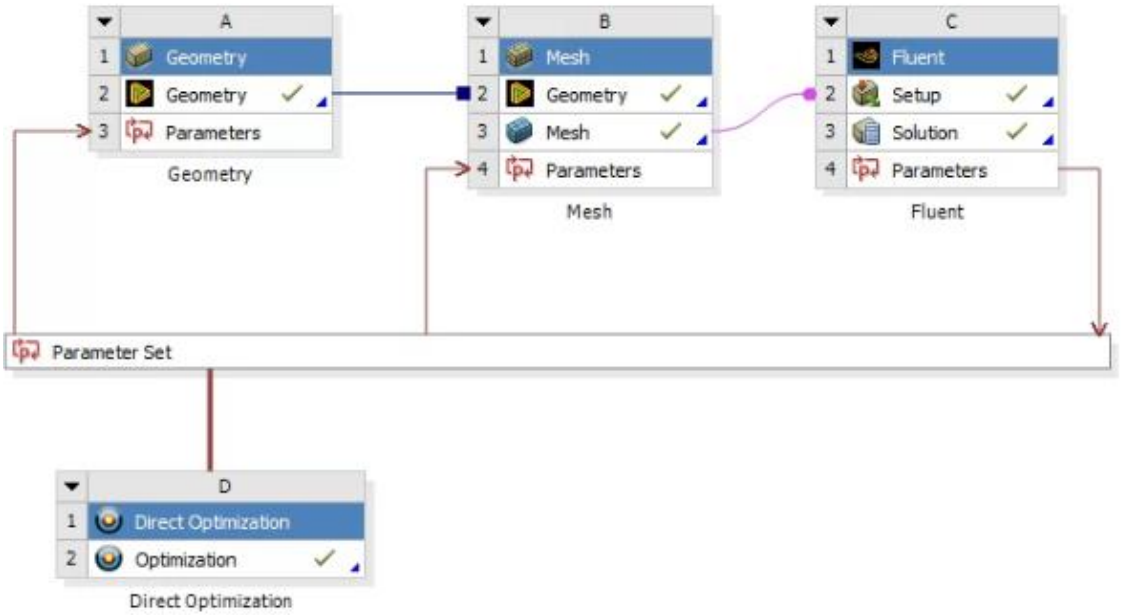

Figure 3.10. Optimization loop in Workbench.

By connecting this block to the previous ones, the software will automatically repeat the previous steps (geometry generation, mesh generation and simulation) for all the generated design points until finding an optimal solution.

Subsequently, it was necessary to choose an optimization method. Within *Workbench*, a variety of methods are available, including Screening, Mixed-Integer Sequential Quadratic Programming (MISQP), Non-Linear Programming by Quadratic Lagrangian (NLPQL), Adaptive Single Objective (ASO), and Multiple Objective Genetic Algorithm (MOGA). Among these, only Screening and ASO are suitable for this specific optimization problem.

Screening is a direct, non-iterative method typically used as an initial sampling approach, while ASO is a gradient-based algorithm that yields a well-defined, global optimization outcome. Both methods were applied to the optimization problem, but as previously described, ASO delivers a more refined optimization result. Hence, ASO was chosen for further evaluation.

The ASO approach operates on the principle of optimal space filling. This method maximizes the distance between sample points to achieve a more uniform distribution in the design space,

effectively filling it with minimal sample points, thereby capturing more information within the design space (Li *et al.*, 2022). In Figure 3.11, the schematic representation of the ASO method is represented.

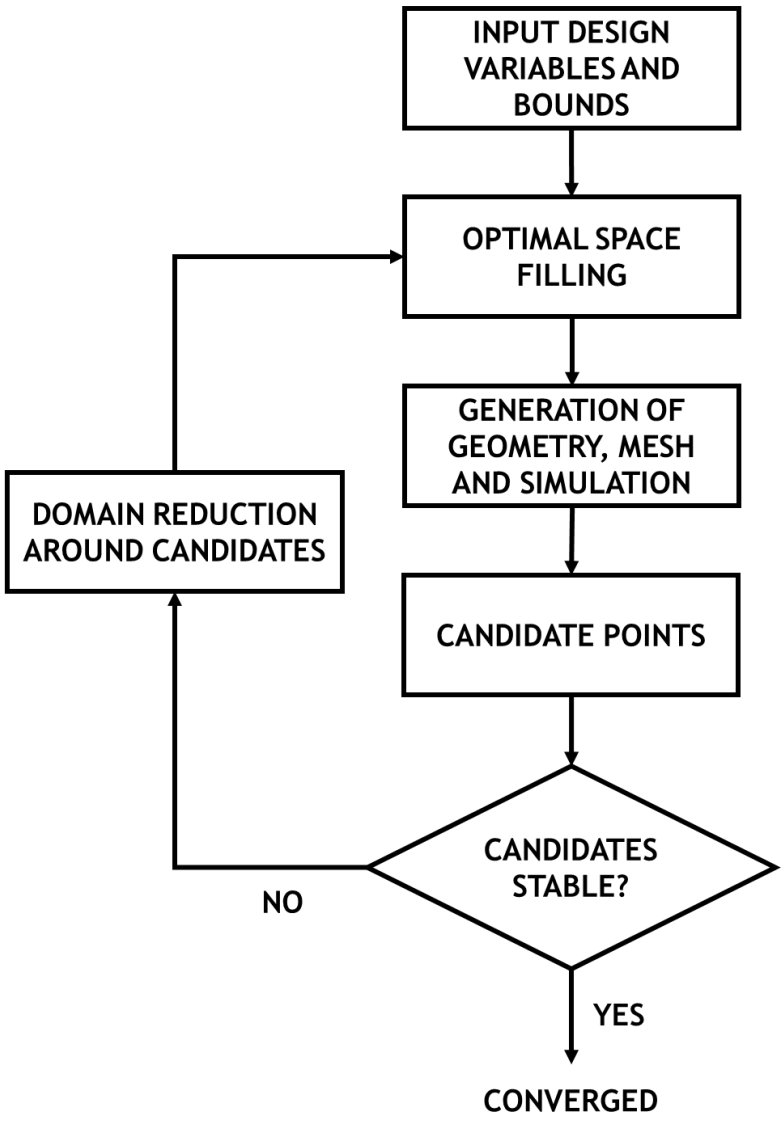

Figure 3.11. Scheme of the ASO method; adapted from (Li et al., 2022).

In this optimization process, 23 initial samples were generated, and its final objective was to find 3 candidates in a maximum of 500 evaluations and 20 domain reductions (values set by default in the software). The convergence tolerance was set to 1×10^{-4}, which provides reliable results and does not significantly increase the computation time. Following the initial sample results, the software automatically adjusts the reduced design space based on the prior optimization results and re-preforms the experimental design.

Before initializing the optimization loop, it is necessary to establish the objective function. In this particular scenario, the optimization problem has a single objective: the maximization of

CH_4 conversion (output parameter previously defined in *Fluent*). The next step involves defining the upper and lower bounds of the parameters, represented in Table 3.3.

Table 3.3. Lower and upper bounds of the input parameters.

PARAMETER	LOWER BOUND	UPPER BOUND
P1	0.5 mm	4 mm
P2		
P3	0.1 mm	16 mm
P4	5	16 mm
P5	90°	150°

The definition of these bounds is extremely important as it serves as the foundation for generating practical design points.

4 Results and discussion

4.1 Method Validation – Tracer Experiments

4.1.1 Laboratorial Results

In the laboratory setup previously described (section 3.1), the fluid flow rate can be tuned by regulating the rotational speed, ω, of the peristaltic pump. During the present work, three different levels of rotational speed were considered: 30 rpm, 40 rpm and 50 rpm. In order to determine the corresponding flow rate values, for each tracer experiment, the time taken to collect a specific fluid volume in the beaker was measured (Appendix B).

Based on the flow rate values obtained (Q) and knowing the cross-sectional area of the inlet of the vessel, the fluid velocity was determined, enabling the calculation of the Reynolds number (Re) using Equation (2.6). The calculation of the Reynolds number holds significant importance for the later simulation inputs. For this calculation, it was assumed that the properties of indigo carmine solution (which is quite diluted in water) were approximately equivalent to those of water at the employed conditions, thus $\rho = 998.2$ kg·m^{-3} and $\mu = 0.001$ Pa·s. Table 4.1 presents the calculated values of Q and Re.

Table 4.1. Values of the volumetric flow rate and Reynolds number for each test.

ω / rpm	Q / m^3·s^{-1}	Re
30	5.68×10^{-7}	64.64
40	7.37×10^{-7}	83.88
50	9.43×10^{-7}	107.28

Based on the evolution of the absorbance of the outlet stream measured during the tests, it became feasible to establish a relationship between this value and the normalized concentration of tracer exiting the system. This relationship is based on the Lambert-Beer Law, which states that the absorbance is directly proportional to the concentration of solute in the solution. Firstly, the spectrophotometer was calibrated with pure water in the cell, and this corresponded to the value of zero absorbance, and as the concentration of tracer in the outlet was increasing, the absorbance was also increasing. Hence, when the value of absorbance reached its maximum, the concentration of tracer on the outlet was equal to the concentration of the mother solution used as tracer. With this relationship, it is possible to depict the evolution of the normalized concentration of tracer, i.e., the Danckwerts' *F* curve, represented in Figure 4.1 for each experiment, at different flow rates.

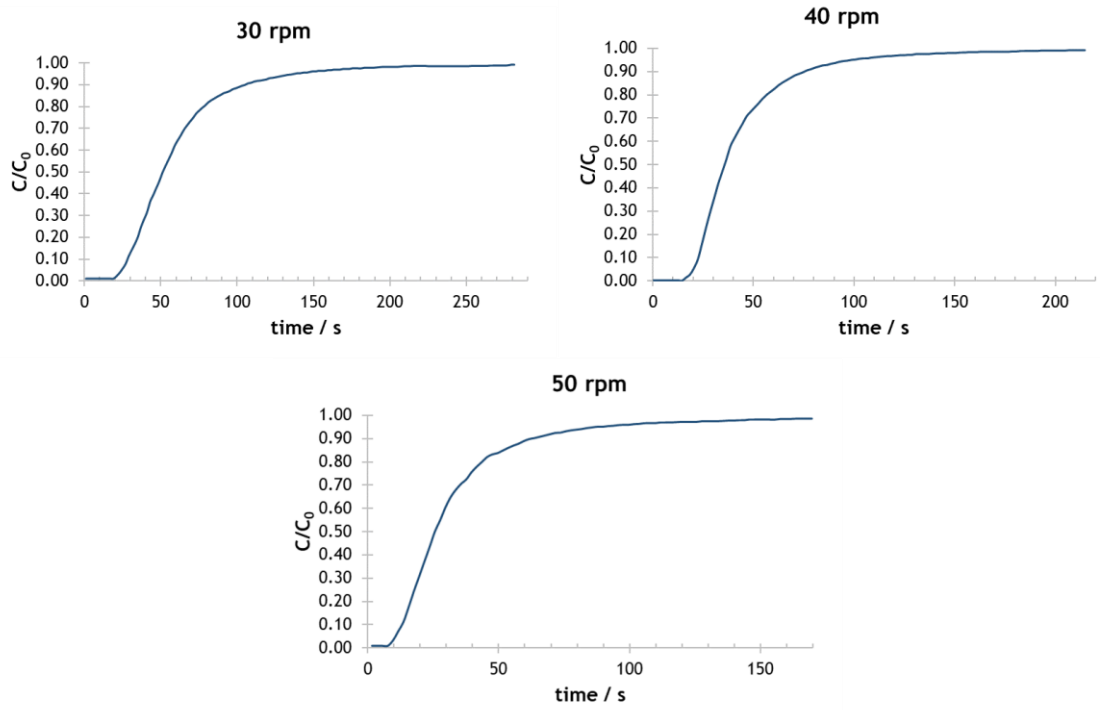

Figure 4.1. F(t) curves for the three tests.

As expected, the curves in Figure 4.1. have a shape characteristic of a response to a step input disturbance. By computing the derivative of the aforementioned curves, it is possible to obtain the RTD curves (E(t)), represented in Figure 4.2.

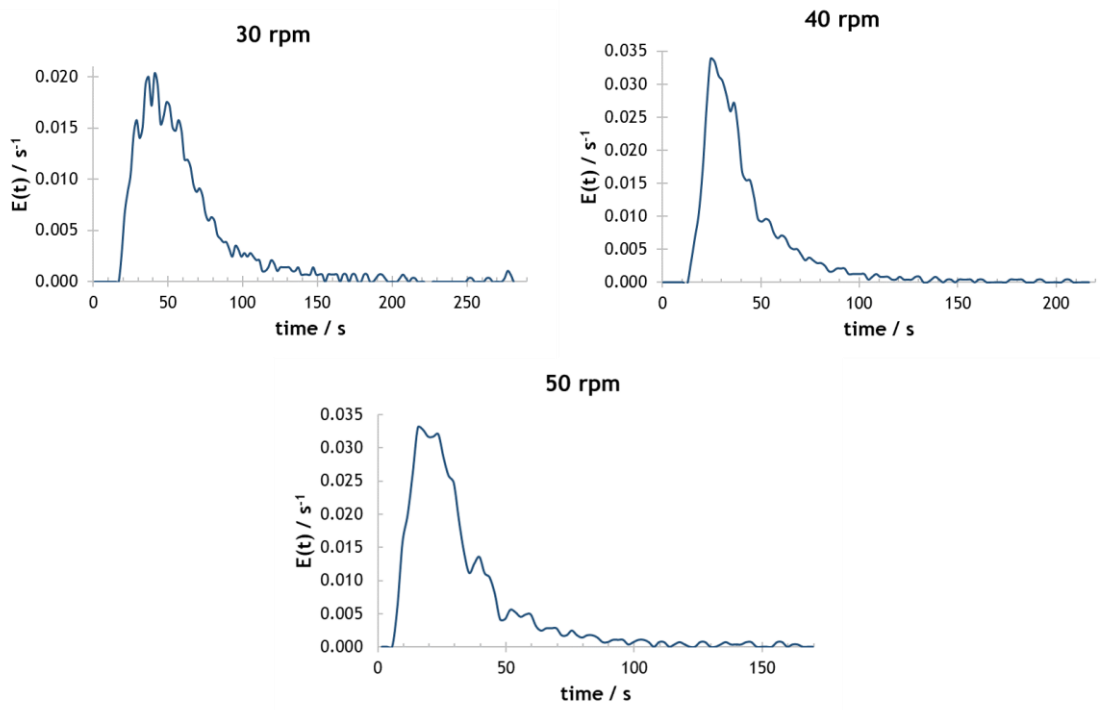

Figure 4.2. Residence time distribution curves for the three tests.

The E(t) curve provides a very important insight into the fluid flow distribution within the system. Hence, by examining these plots, it becomes possible to identify the time at which the tracer starts to exit the fluid domain (corresponding to the start of the peak) and the time when only tracer is leaving the reactor (corresponding to the end of the peak). To calculate the mean residence time, the area under the $t \cdot E(t)$ curve was determined using the trapezoid rule.

Following the completion of all tests, the liquid contained within the reactor was transferred to a beaker, allowing for the measurement of the corresponding fluid volume, which was determined to be 32.0 mL. With this volume value at hand, it became feasible to calculate the space time of the reactor for each test using Equation (2.10). The values of τ and $\bar{t_r}$ are represented in Table 4.2.

Table 4.2. Calculated values of τ and $\bar{t_r}$ for the three tests.

Test	30 rpm	40 rpm	50 rpm
τ / s	56.30	43.39	33.93
$\bar{t_r}$ / s	59.46	42.98	31.64

As it is possible to see, the mean residence time is higher than the space time in test executed for a rotational speed of 30 rpm. On the other hand, for the other two tests, the mean residence time is lower than the space time.

Regarding the two congruent tests (those at higher flow rates), and as previously mentioned, $\bar{t_r} < \tau$ means that there are dead or recirculation zones inside the vessel. As for the results of the 30 rpm test, this discrepancy can be justified by inaccuracies intrinsic to some measurements, such as the volume of the liquid contained inside the vessel, the delay in the tubing and the flow rate measurements.

These runs were recorded, allowing for a visual representation of the tracer's behavior within the vessel (Appendix C). Figure 4.3 presents selected frames from the video footage captured during the tests, specifically capturing the moment when the initial elements of fluid are reaching the outlet of the domain (fluid flow is from left to right of each image).

Figure 4.3. Frames of the video taken for the three tests when the first elements of fluid leave the domain: A) ω = 30 rpm; B) ω = 40 rpm; C) ω = 50 rpm.

Upon careful examination of Figure 4.3, it is possible to see that in the central region of the reactor the fluid traverses the obstacles at a notably faster rate compared to the zones in proximity to the borders. This phenomenon should ideally manifest as distinct peaks in the E(t) curves for the different experiments. However, due to the inherent experimental noise associated with the spectrophotometer and the relatively large time step between absorbance measurements (2 s), it becomes challenging to discern these distinct peaks in the E(t) curves.

4.1.2 Simulation results

In order to replicate the experimental conditions into the simulation setup, the previously calculated values of volumetric flow rate were utilized to determine the velocity of the tracer at the inlet, v_{in}. Following the initialization of the simulation, a *Surface Report* of the *Volume Flow Rate* at the outlet was computed for each simulation, enabling a comparison with the corresponding experimental values. Table 4.3 presents the defined velocity values in the boundary conditions, as well as the volumetric flow rates computed from the simulation software.

Table 4.3. Values of v_{in} and Q computed in Fluent for each simulation.

Test	A	B	C
v_{in} / m·s^{-1}	7.58×10^{-3}	9.83×10^{-3}	1.26×10^{-2}
Q / m^3·s^{-1}	5.70×10^{-7}	7.37×10^{-7}	9.44×10^{-7}

Proceeding to the post-processing stage, it was possible to retrieve the graphic contours of the velocity magnitude. Figure 4.4 depicts those contours for the three tests.

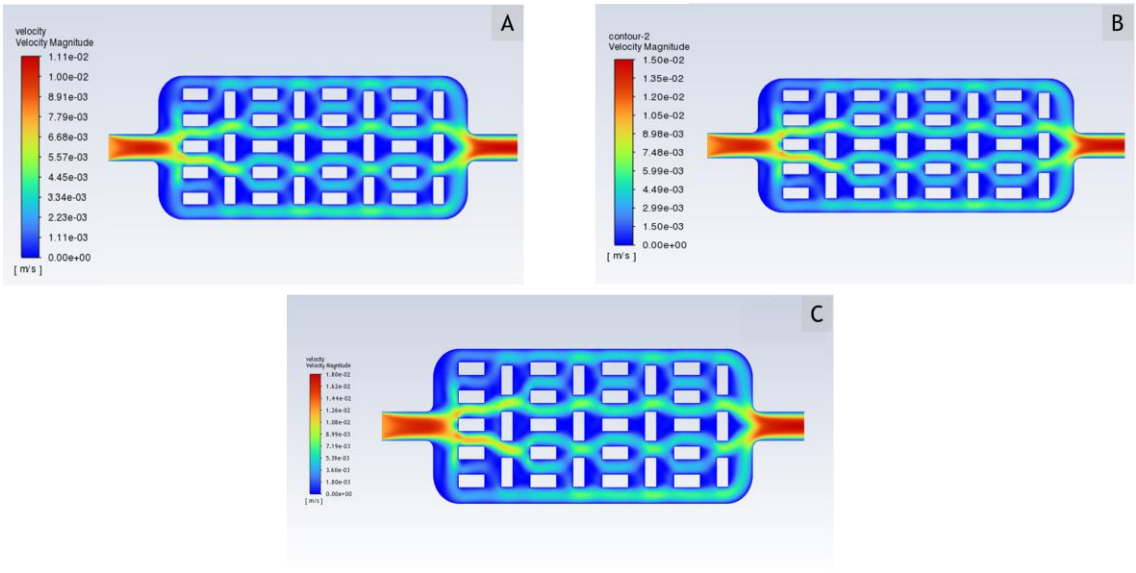

Figure 4.4. Velocity magnitude contours for different inlet fluid velocities: A) v_{in} = 7.58×10^{-3} m·s^{-1}; B) v_{in} = 1.04×10^{-2} m·s^{-1}; C) v_{in} = 1.26×10^{-2} m·s^{-1}.

Analyzing Figure 4.4, it is apparent that the velocity exhibits greater values at both the inlet and outlet of the domain, which aligns with expectation given the smaller cross-sectional area in these areas when compared to the body of the vessel. Additionally, the velocity magnitude in the central region is notably higher when compared with the values near the walls. This could be a sign of the existence of preferential paths, which can be confirmed by the contours of mass fraction of tracer. Figure 4.5 represents the tracer contours for three different times compared to the space time in each case: 0.5τ, τ, and 5τ.

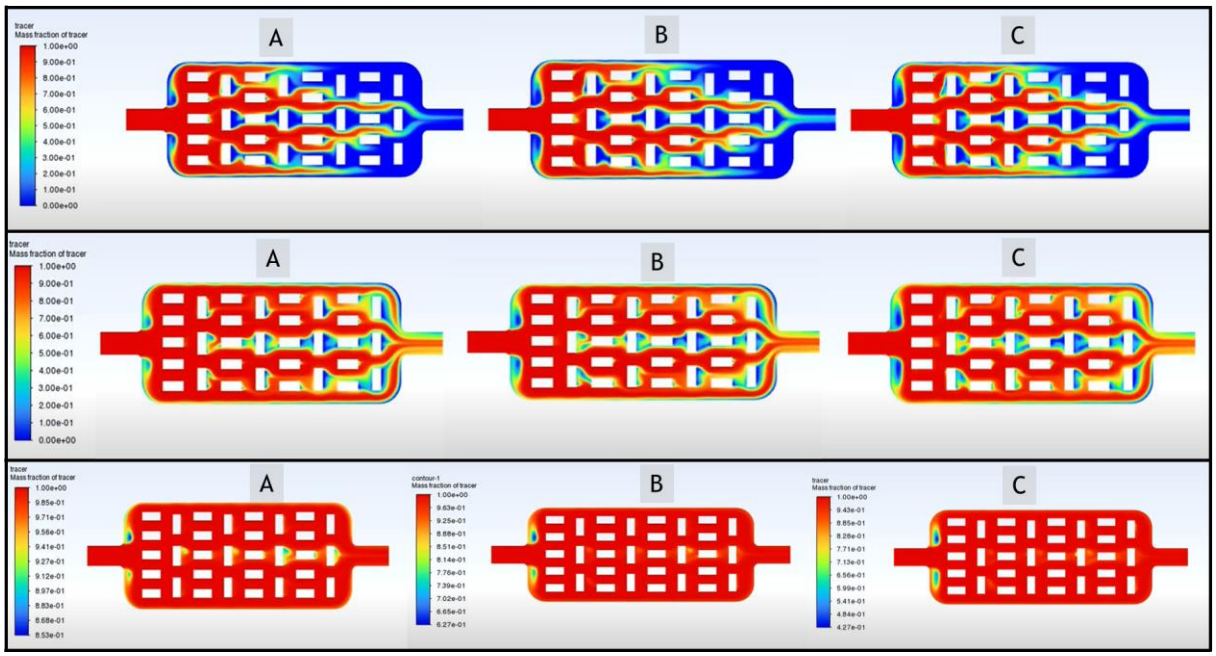

Figure 4.5. Contours of mass fraction of tracer for 0.5τ (up), τ (middle) and 5 τ (down) for all tests: A) v_{in} = 7.58×10^{-3} m·s^{-1}; B) v_{in} = 1.04×10^{-2} m·s^{-1}; C) v_{in} = 1.26×10^{-2} m·s^{-1}.

As it is possible to observe for 0.5τ, in the center region the fluid transverses the obstacles at a faster rate than near the walls, as was predicted in the velocity contours. Additionally, it is possible to observe an asymmetry in the flow pattern (evident when comparing the distribution of fluid near the walls), suggesting a potential asymmetry in the geometry upon its creation in *DesignModeler*.

Analyzing the other contours, it is possible to assess that there may be recirculation zones within the domain, especially near the inlets and the obstacles in the center region. It is also expected that these recirculation areas have higher values for test C, where the velocity is higher.

For each one of these simulations, the normalized concentration of tracer at the outlet was extracted in order to allow the computation of the Danckwerts' F(t) curves, represented in Figure 4.6.

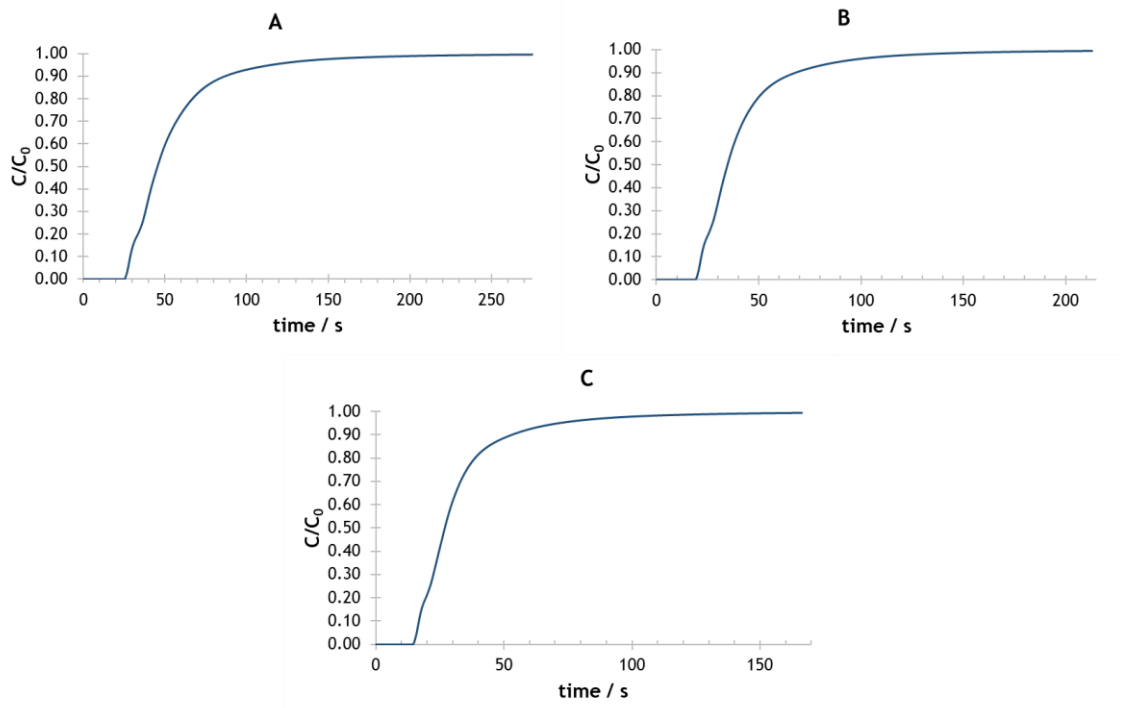

Figure 4.6. Danckwerts' F(t) curves for the tests: A) v_{in} = 7.58×10^{-3} m·s^{-1}; B) v_{in} = 1.04×10^{-2} m·s^{-1}; C) v_{in} = 1.26×10^{-2} m·s^{-1}.

Once again, the F(t) curves represent the characteristic response to a step disturbance. Proceeding analogously to the experimental part, the E(t) curves were obtained by calculating the derivative of the respective numerical F(t) curve, represented in Figure 4.7.

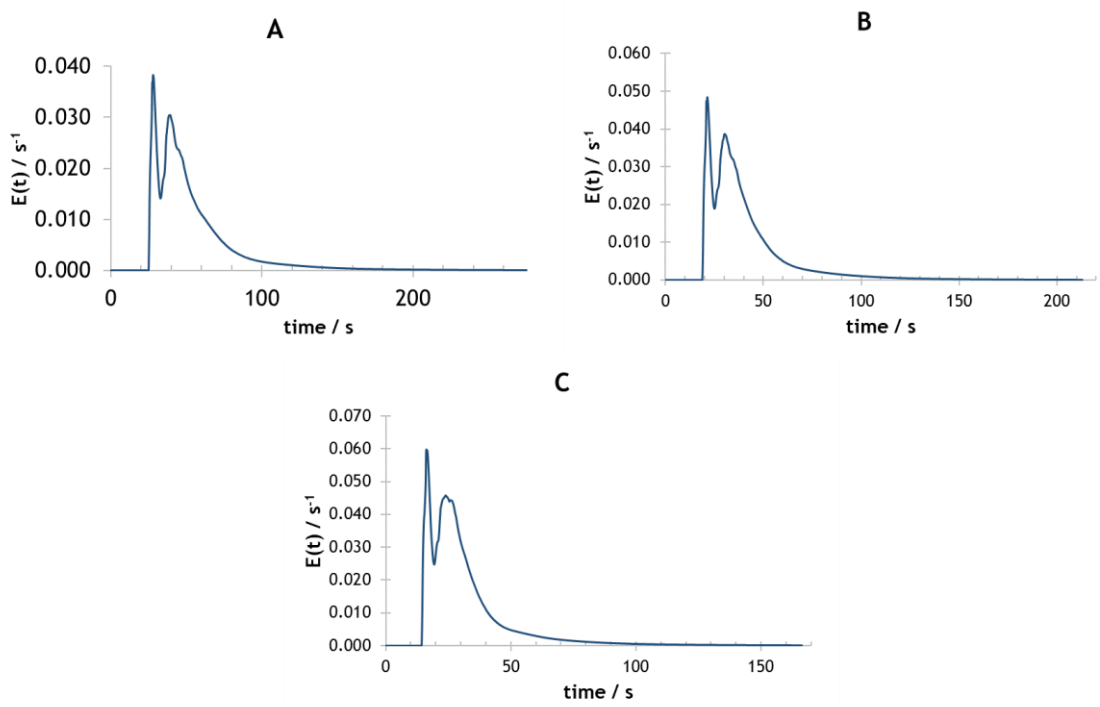

Figure 4.7. Residence time distribution curves for the tests: A) v_{in} = 7.58×10^{-3} m·s^{-1}; B) v_{in} = 1.04×10^{-2} m·s^{-1}; C) v_{in} = 1.26×10^{-2} m·s^{-1}.

Analyzing Figure 4.7, it is visible that a portion of the fluid exits the reactor earlier, indicating the presence of preferential flow pathways within the fluid domain.

Once again, by calculating the area beneath the $t \cdot E(t)$ curve, the value of $\overline{t_r}$ was determined. The *Fluent* software allows to report a *Surface Integral* in order to compute the volume of the domain, obtaining a value of 3.14×10^{-5} m^3. Utilizing this volume value, the space time can be calculated using Equation (2.10). The values of τ, $\overline{t_r}$ and $^{V_d}/_{V}$ are represented in Table 4.4.

Table 4.4. Calculated values of τ, $\overline{t_r}$ and $^{V_d}/_{V}$ for the simulations.

Test	A	B	C
τ / s	55.09	42.59	33.26
$\overline{t_r}$ / s	53.69	41.10	31.74
$^{V_d}/_{V}$ / %	2.53	3.49	4.57

Upon examination of these values, it is possible to assess that, in all tests, $\tau > \overline{t_r}$. This indicated the presence of a dead or stagnant volume zone within the system. Upon examination of the $^{V_d}/_{V}$ values, it is possible to confirm the previous assertion: with an increase in the volumetric flow rate, the dead volume fraction also increases.

4.1.3 Experimental vs Simulation

The primary objective of this section is to validate the applicability of the CFD approach by a comparison between simulation and experimental data. For this purpose, the F(t) curves (both experimental and simulation) were plotted together for graphical comparison in Figure 4.8.

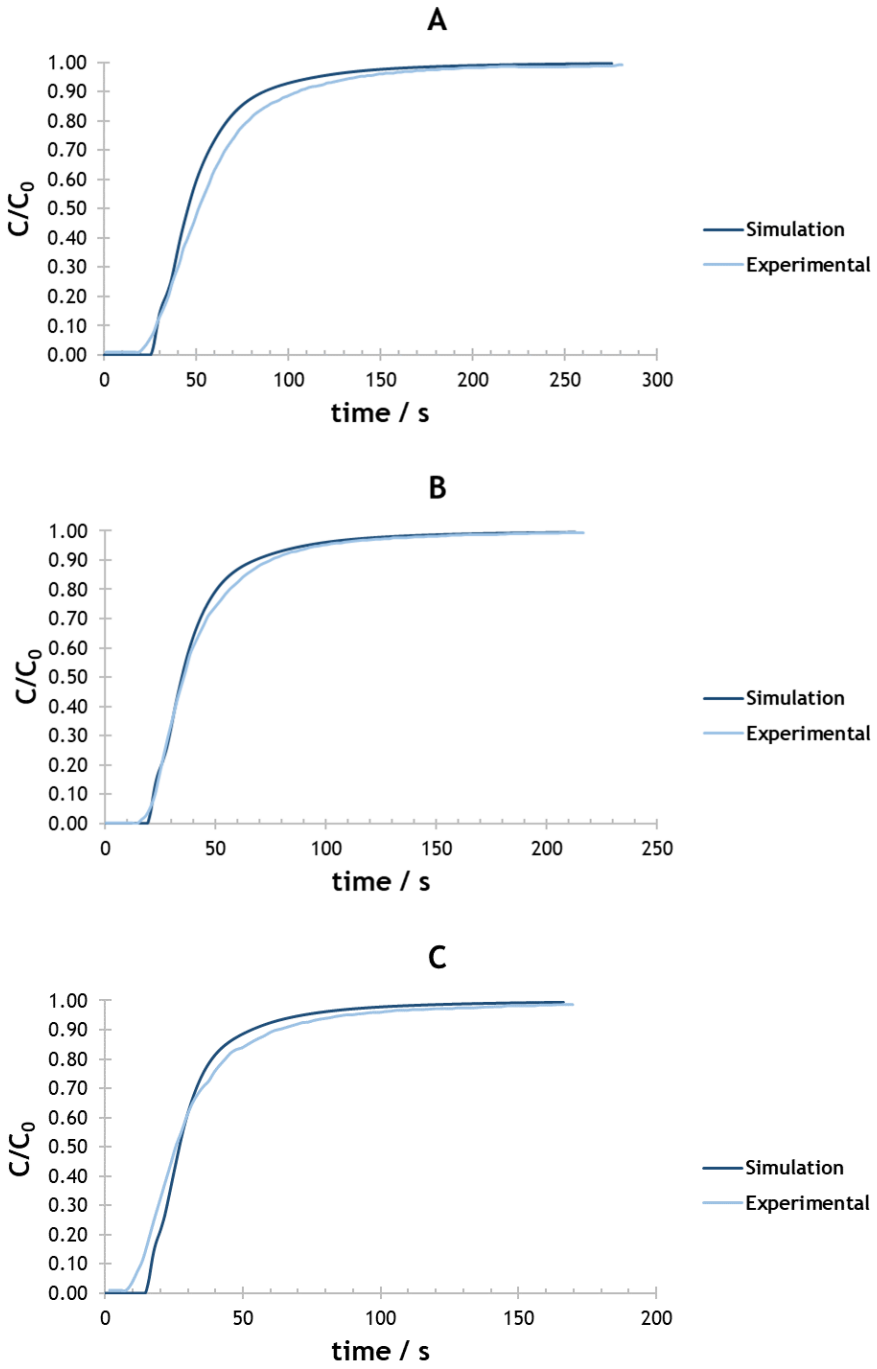

Figure 4.8. F(t) curves for the experimental and simulation runs at different inlet velocities: A) v_{in} = 7.58×10^{-3} m·s^{-1}; B) v_{in} = 1.04×10^{-2} m·s^{-1}; C) v_{in} = 1.26×10^{-2} m·s^{-1}.

In Figure 4.8, it can be interpreted that the tracer departs earlier from the vessel in the experimental tests and exhibits a slower ascension. In contrast, the simulation shows a more

abrupt increase of tracer concentration at the outlet. The dissimilarity in the timing can be related to the uncertainty in the time measurement of the delay caused by the tubes. Additionally, the disparity in the ascension characteristics of the curves can be accounted for the definition of the mass diffusivities, implying different levels of mass dispersion. As previously mentioned, the simulation was configured with a default value for the mass diffusivity of the mixture, which may not accurately correspond to the real value of the tracer aqueous solution.

To allow a simpler comparison, the calculated values of Q, τ and $\overline{t_r}$ were compiled in Table 4.5.

Table 4.5. Calculated values of Q, τ and $\overline{t_r}$ for the experimental and simulation tests.

TEST		EXPERIMENTAL	SIMULATION	DEVIATION (%)
A	Q / $m^3 \cdot s^{-1}$	5.68×10^{-7}	5.70×10^{-7}	0.4
	τ / s	56.30	55.09	2.1
	$\overline{t_r}$ / s	59.46	53.69	9.7
B	Q / $m^3 \cdot s^{-1}$	7.37×10^{-7}	7.37×10^{-7}	0.1
	τ / s	43.39	42.59	1.9
	$\overline{t_r}$ / s	42.98	41.10	4.4
C	Q / $m^3 \cdot s^{-1}$	9.43×10^{-7}	9.44×10^{-7}	0.1
	τ / s	33.93	33.26	2.0
	$\overline{t_r}$ / s	31.64	31.74	0.3

Analyzing Table 4.5, it is possible to confirm that the values for both the experimental and the simulation show the existence of recirculation zones within the domain, with the exception of the 30 rpm experimental test. The disparities between the experimental and simulation results can be attenuated by changing some inputs:

- Changing the type of pump. Peristaltic pumps are not able to provide a consistently steady flow rate.
- Finding more efficient measurement methods for the delay in the tubing, the volumetric flow rate, and the volume of liquid inside the vessel.
- Adapting the simulation inputs to the reality. In this experiment, the properties of the tracer were considered to be almost equivalent to water, which might not be true.

- Adapting the geometry of the printed vessel to the connections between the tubes and the vessel in a more efficient way to prevent leakage.

Overall, and considering these experimental sources of error, it is possible to assess that the method has been effectively validated since the deviation between the values is on average 0.76 % and does not exceed 10 % (this value is associated with the 30 rpm test, which was concluded that would not be a reliable result).

4.2 Optimization Approach

As aforementioned, an automated optimization tool was employed with the aim of maximizing CH_4 conversion. Figure 4.9 illustrates the progression of conversion throughout the optimization process after 200 iterations.

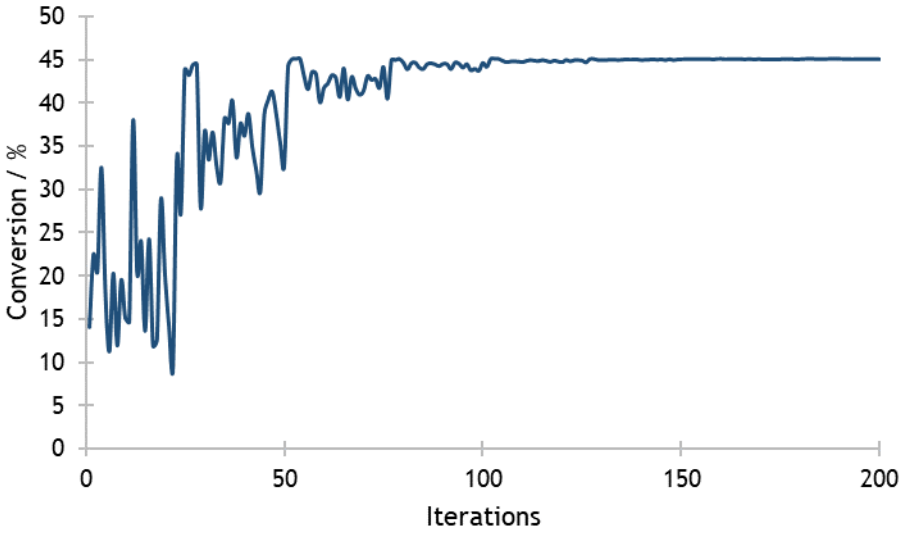

Figure 4.9. History of methane conversion.

It is evident that the conversion value begins to converge toward a specific value, a result of the domain reductions explained earlier in section 3.2. Detailed history plots for the design parameters, along with their respective upper and lower bounds can be found in Appendix D.

Following the calculation, the software generates three candidate points, which are presented in Table 4.6.

Table 4.6. Candidate points generated by the software.

Candidate Point	P1 / mm	P2 / mm	P3 / mm	P4 / mm	P5 / °	Conversion / %
1	2.6674	1.3703	0.12308	15.998	149.98	45.145
2	2.5139	1.1783	0.55961	15.796	143.18	42.807
3	2.6025	0.5809	0.85319	14.364	136.12	38.265

To facilitate a clearer comprehension of these values, Figure 4.10 provides a graphical representation showcasing the candidate points and the corresponding input values.

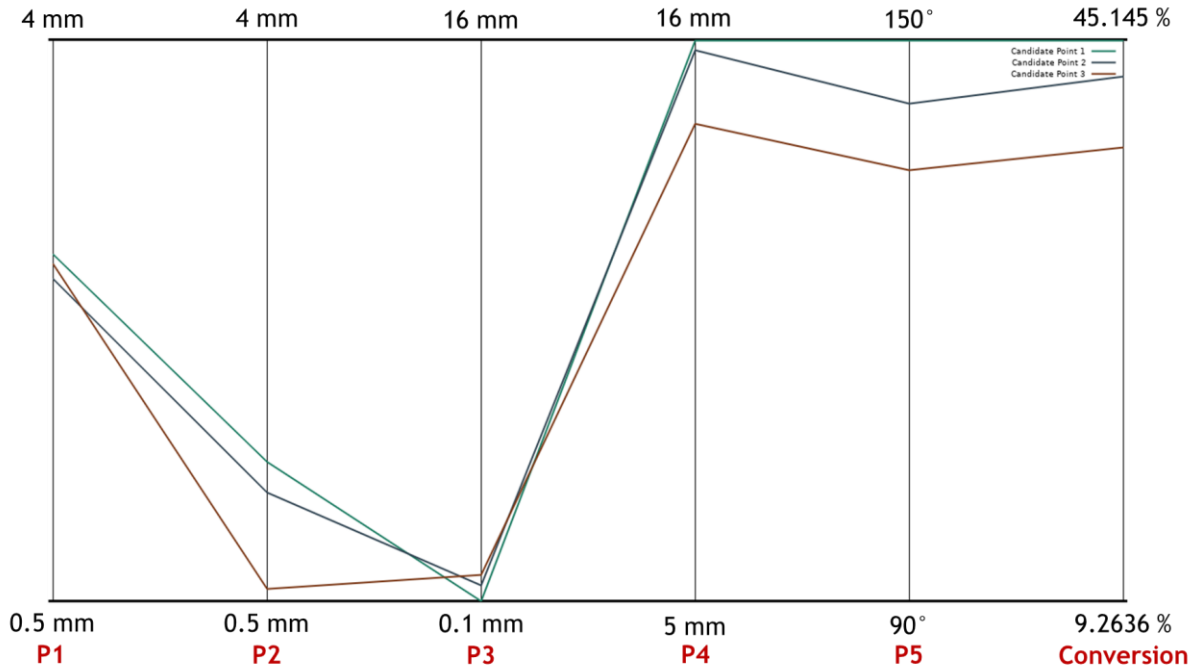

Figure 4.10. Graphical representation of the candidate points.

Examining the figure above, it becomes evident that, for all candidate points, P3 tends toward the minimum value (it was varied in the range 0.1-16 mm), whereas the values of P4 and P5 tend toward their maximum value (varied in the ranges 5-16 mm and 90-150º, respectively - Table 3.3). However, the dimensions of the obstacles (P1 and P2) do not appear to converge to a limiting value.

In the following analysis, the main focus will be in candidate point 1, given its higher conversion value. Figure 4.11 portrays the geometry proposed for this candidate point.

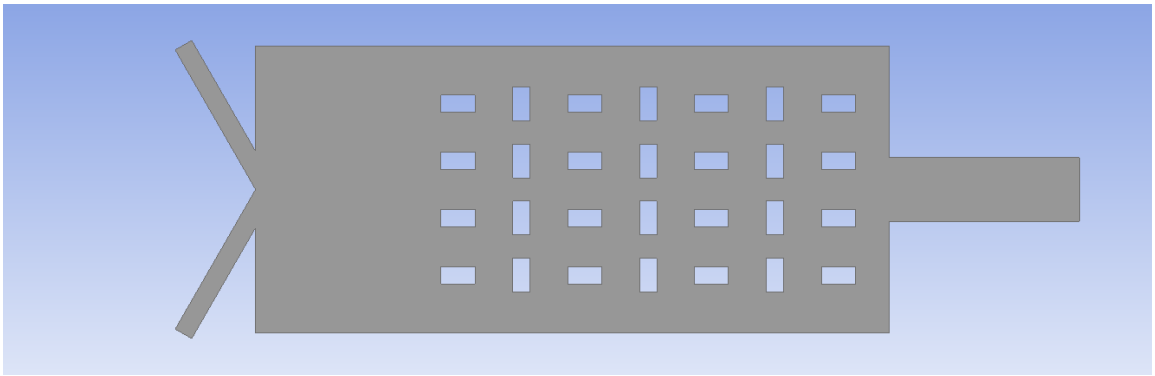

Figure 4.11. Geometric model of candidate point 1.

When comparing this model with the initial guess (Figure 3.9), that had a CH_4 conversion of 11.16%, several notable differences become apparent. In the optimized model, the obstacles

are smaller, the inlets are closer and more inclined and there is an increased distance between the inlets and the catalytic surfaces. The simulation was conducted using the values of candidate point 1 to facilitate a more in-depth analysis. Figure 4.12 depicts the contours of velocity magnitude for both the initial guess and the optimized model.

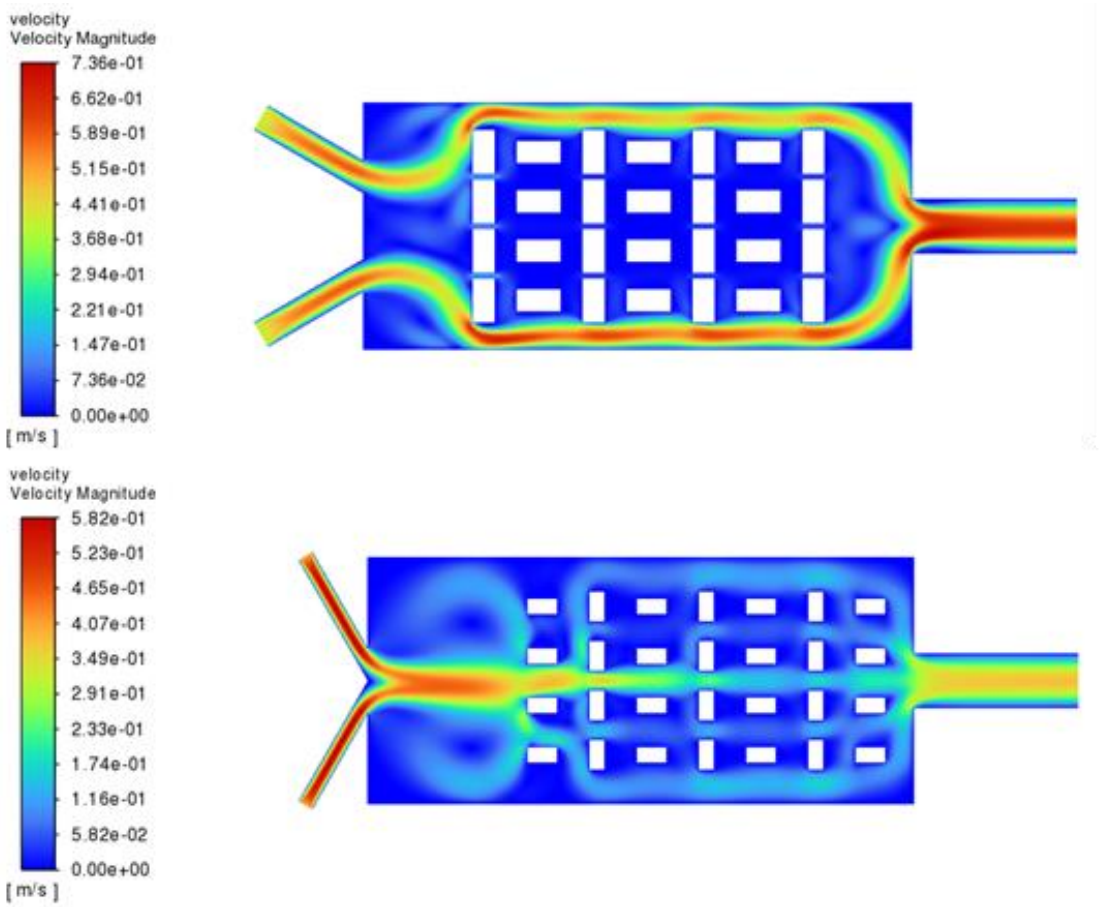

Figure 4.12. Contours of velocity of the initial guess (up) and the optimized model (down).

Comparing both contours, it becomes evident how the dimension of the obstacles affects the flow distribution. Smaller obstacles enable the fluid to pass through them, diverting it away from the exterior walls as occurs in the initial guess. Also, larger obstacles may lead to undesirable pressure drop issues, which is not desirable for the functioning of a reactor. Examining the other parameters, having the inlets more inclined and positioned closer to each other allows to redirect the fluid flow towards the centre of the reactor, enhancing the mixture levels.

Subsequently, the contours of the normalized concentration of all reaction compounds were retrieved. Figure 4.13 depicts the normalized concentration contours for the reactants.

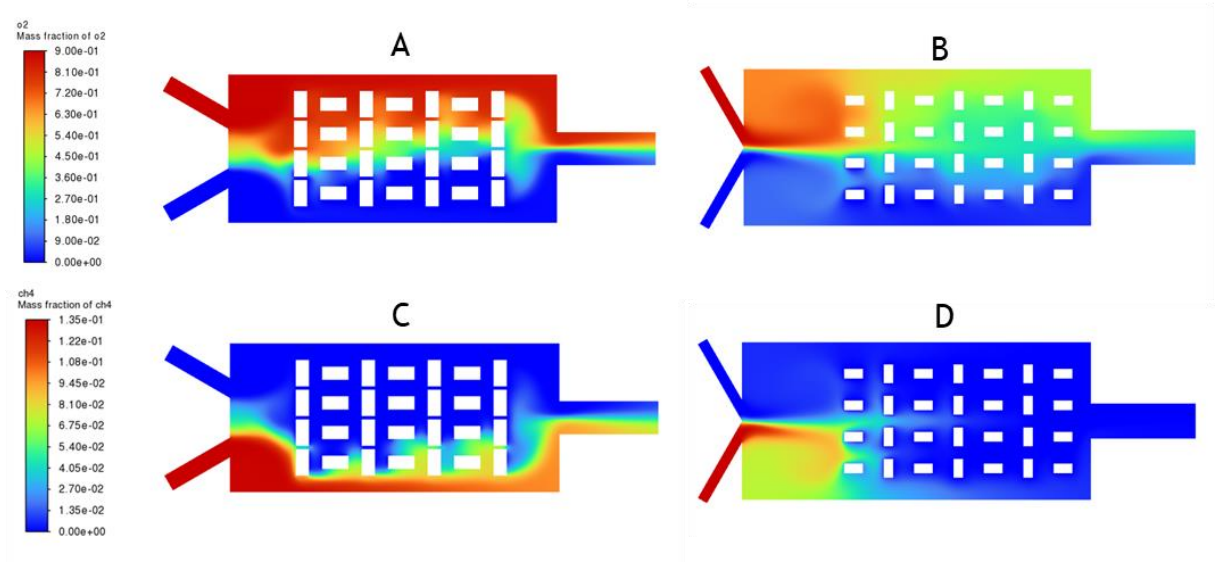

Figure 4.13. Contours of normalized concentration: A) for O_2 in the initial guess; B) for O_2 in the optimized model; C) for CH_4 in the initial guess; D) for CH_4 in the optimized model.

Examining Figure 4.13, it is evident that in the initial guess, the reactants predominantly accumulate at the borders of the reactor, a pattern consistent with the velocity contours, indicating limited mixing. Contrasting this with the optimized model, a significant improvement is observed. In the optimized model, nearly all CH_4 has reacted, as evidenced by the contours showing CH_4 only near the inlets where the reaction does not occur since it does not exist any catalytic surface. This analysis also confirms that O_2 disperses more effectively throughout the reactor and reaches its bottom, as the reaction needs the presence of both reactants.

Figure 4.14 depicts the contours of normalized concentration for the products of the reaction.

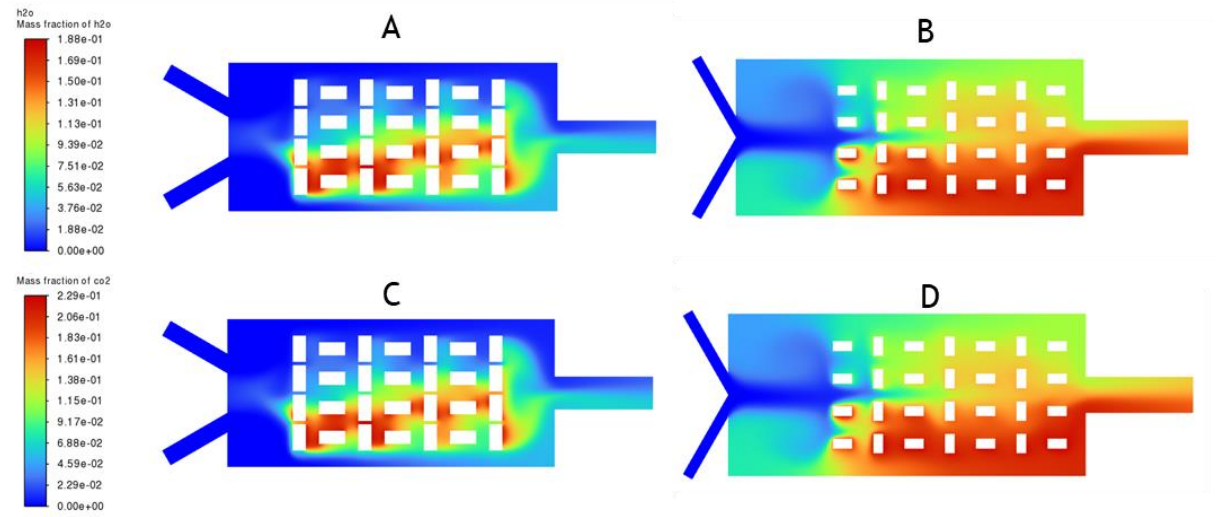

Figure 4.14. Contours of normalized concentration: A) for H_2O in the initial guess; B) for H_2O in the optimized model; C) for CO_2 in the initial guess; D) for CO_2 in the optimized model.

Finally, examining the product concentration contours, it is clear that the concentration of products is significantly higher in the optimized structure. Firstly, the use of smaller obstacles in the optimized design facilitates the easier spread of products throughout the reactor. Secondly, the optimized configuration improved mixing, achieved through the high inclination and proximity of the inlets and their greater distance from the catalytic surfaces. This setup ensures a greater contact between the two reactants and the catalytic surfaces, leading to the increased conversion of the reactants into products.

5 Conclusions

The chemical industry relies heavily on the optimization of its process units. CFD has emerged as a powerful tool for analyzing fluid flow and addressing heat and mass transfer challenges. Combining CFD analysis with design optimization is a valuable approach for achieving the highest efficiency. However, traditional CFD analysis may not always consider manufacturing costs when dealing with complex geometries. This is where AM plays a pivotal role, offering nearly unrestricted freedom for producing complex geometries.

This work embodied two distinct stages: the validation of the CFD solver and the optimization of the reactor model. Firstly, a 3D Printed model was employed in laboratorial tracer experiments, enabling the replication of these experiments within the simulation software. This step aimed to assess the reliability of the solver. Subsequently, an optimization was employed for an illustrative structured packed reactor design, with the objective of enhancing the reactor performance.

In the laboratory, the tracer experiments were conducted using water and a solution of indigo carmine (tracer) for three different flow rates. The outlet flow from a vessel filled with obstacles was analyzed with a spectrophotometer, which allowed to establish a relationship between the absorbance of the outlet stream and the concentration of tracer. Later, these tracer experiments were replicated in the simulation software.

Analyzing the results, it is possible to infer that the CFD solver can accurately predict these fluid flow phenomena, yet with some observed disparities. These disparities can be addressed by the adjustment of the laboratorial protocol and setup, since some measurements are prone to inaccuracies, and the adjustment of some simulation inputs since some parameters are chosen by default and may not correspond to reality (e.g., mass diffusivity coefficient).

The last step of this work was to employ a surface reaction in a structured packed reactor. The chosen (model) reaction was the oxidation of methane, and the main objective was to optimize geometric parameters to maximize the conversion of methane (limiting reactant). For the optimization, the Direct Optimization feature in Workbench was employed by using the ASO method.

This method was successfully employed and revealed interesting results. It was found that the inlets disposition had great impact on the initial mixing of the reactants; closer and more inclined inlets lead to a greater contact between the two different compounds. This mixing was also influenced by the distance between the inlets and the catalytic surfaces, where a higher distance would be more beneficial. As for the obstacle's dimensions, it was possible to see that it had a great impact on the dispersion of compounds within the reactor.

In conclusion, all objectives of this study have been achieved. It is thereby plausible to reckon that the synergistic application of CFD analysis, optimization and AM presents a powerful tool, capable of significantly progressing innovations in the design of process units (e.g. chemical reactors).

6 Assessment of the work done

6.1 Objectives Achieved

The primary objectives of this work were successfully fulfilled. In a first stage, the main focus was on method validation through the execution of tracer experiments on a laboratorial scale, followed by the replication of the same process through simulation. The method validation was successful, although for closer alignment between the results, potential adjustments to the simulation setup and laboratory procedures could be considered.

In the second phase of this work, the central aim was to implement an optimization process for geometric parameters with the ultimate goal of improving reactor performance in the oxidation of methane by maximizing its conversion. This optimization approach was successfully implemented, revealing a high potential for optimization problems.

6.2 Future Work

As aforementioned, the present work intended to provide a preliminary insight on the potential of combining additive manufacturing, computer-aided design, and specific CFD/optimization tools.

In the very short term, the combination of tools addressed in this work can be much more explored, especially regarding the optimization part. This work only focused on maximizing the conversion of a reactant in a catalytic reactor. However, within this same scenario, it would be relevant to extend the analysis to other features - such as pressure drop, mixing terms and heat transfer/energy parameters - since the overall performance of a reactor is also dependent of these features; this is particularly in strongly exothermal reactions, like the one chosen herein. The external geometry and configuration of the reactor could also be changed, especially the shape of the obstacles and the disposition of the inlets.

As for the experimental/validation part, firstly, the laboratorial protocol should be improved, as previously stated. Different types of experiments involving 3D printed vessels could also be thought – for example, experimental tests involving heat transfer effects. Additionally, the recent availability of a wide range of materials in 3D printing is another aspect to explore.

In a more general perspective, and in a longer term, the approach used on this work has the potential to be successfully adapted to a wider range of scales, reaction systems, and other types of units/devices.

6.3 Final Assessment

The overall outcome of this work is highly positive, offering a wide range of new skills. Personally, it was a challenging experience as it covered diverse subjects. In addition, it provided an opportunity to embark on beyond the limits of the course and delve into new domains of engineering, including modeling and computer-aided design.

7 References

Ahmad, H., and Fauzuddin Ayob. 2017. "State of the Art Review of the Application of Computational Fluid Dynamics for High Speed Craft." *Journal of Ocean, Mechanical and Aerospace* 39.

Amores, Isabel Diañez, Joamin González-Gutiérrez, I. Martínez García, José M. Franco, and Críspulo Gallegos. 2022. "3D printing – Present and future – A Chemical Engineering perspective." *Chemical Engineering Research and Design* 187: 598-610. https://doi.org/https://doi.org/10.1016/j.cherd.2022.08.049. https://www.sciencedirect.com/science/article/pii/S0263876222004610.

Amwel Enterprises. 2008. "A Brief History of CFD." Accessed 26/04. http://www.amwel.com/history.html.

Anderson, J.D. 1995. *Computational Fluid Dynamics*. Edited by John F. Wendt. 3 ed.: Springer Berlin, Heidelberg.

Aryafar, M., and F. Zaera. 1997. "Kinetic study of the catalytic oxidation of alkanes over nickel, palladium, and platinum foils." *Catalysis Letters* 48 (3): 173-183. https://doi.org/10.1023/A:1019055810760. https://doi.org/10.1023/A:1019055810760.

ASTM, Designation F. 2009. "2792-09. Standard Terminology for Additive Manufacturing Technologies." *ASTM International*.

Aziz, Abdul. 2010. "Hydrodynamic and thermal slip flow boundary layers over a flat plate with constant heat flux boundary condition." *Communications in Nonlinear Science and Numerical Simulation* 15 (3): 573-580. https://doi.org/https://doi.org/10.1016/j.cnsns.2009.04.026. https://www.sciencedirect.com/science/article/pii/S1007570409002019.

Campos, João Moreira de. 2013. *Notas Para o Estudo da Mecânica de Fluidos*. Edited by FEUP Edições.

Capel, Andrew J., Rowan P. Rimington, Mark P. Lewis, and Steven D. R. Christie. 2018. "3D printing for chemical, pharmaceutical and biological applications." *Nature Reviews Chemistry* 2 (12): 422-436. https://doi.org/10.1038/s41570-018-0058-y. https://doi.org/10.1038/s41570-018-0058-y.

Catarino, S., R. Lima, and G. Minas. 2017. "12 - Smart devices: Lab-on-a-chip." In *Bioinspired Materials for Medical Applications*, edited by Lígia Rodrigues and Manuel Mota, 331-369. Woodhead Publishing.

Constales, Denis, Gregory S. Yablonsky, Dagmar R. D'hooge, Joris W. Thybaut, and Guy B. Marin. 2017. "Chapter 3 - Complex Reactions: Kinetics and Mechanisms – Ordinary Differential Equations – Graph Theory." In *Advanced Data Analysis & Modelling in Chemical Engineering*, edited by Denis Constales, Gregory S. Yablonsky, Dagmar R. D'hooge, Joris W. Thybaut and Guy B. Marin, 35-82. Amsterdam: Elsevier.

Danckwerts, P. V. 1953. "Continuous flow systems: Distribution of residence times." *Chemical Engineering Science* 2 (1): 1-13. https://doi.org/https://doi.org/10.1016/0009-2509(53)80001-1. https://www.sciencedirect.com/science/article/pii/0009250953800011.

Eslahpazir, M., C. Wittmann, and R. Krull. 2011. "2.75 - Computational Fluid Dynamics." In *Comprehensive Biotechnology (Second Edition)*, edited by Murray Moo-Young, 1027-1038. Burlington: Academic Press.

Fogler, H. Scott. 1999. *Elements of Chemical Reaction Engineering*. 3 ed.: Prentice Hall.

FormLabs. 2023. "Guide to Stereolitography (SLA) 3D Printing." Accessed 10/07/2023. https://formlabs.com/blog/ultimate-guide-to-stereolithography-sla-3d-printing/.

Gao, Wei, Yunbo Zhang, Devarajan Ramanujan, Karthik Ramani, Yong Chen, Christopher B. Williams, Charlie C. L. Wang, Yung C. Shin, Song Zhang, and Pablo D. Zavattieri. 2015. "The status, challenges, and future of additive manufacturing in engineering." *Computer-Aided Design* 69: 65-89. https://doi.org/https://doi.org/10.1016/j.cad.2015.04.001. https://www.sciencedirect.com/science/article/pii/S0010448515000469.

IdealSimulations. 2020. "Courant Number." https://www.idealsimulations.com/resources/courant-number-cfd/.

Kiss, Anton A., and Robin Smith. 2020. "Rethinking energy use in distillation processes for a more sustainable chemical industry." *Energy* 203: 117788. https://doi.org/https://doi.org/10.1016/j.energy.2020.117788. https://www.sciencedirect.com/science/article/pii/S0360544220308951.

Kreutzer, Michiel T., Freek Kapteijn, and Jacob A. Moulijn. 2006. "Shouldn't catalysts shape up?: Structured reactors in general and gas–liquid monolith reactors in particular." *Catalysis Today* 111 (1): 111-118. https://doi.org/https://doi.org/10.1016/j.cattod.2005.10.014. https://www.sciencedirect.com/science/article/pii/S0920586105007108.

Kumar, S. Anand, and R. V. S. Prasad. 2021. "Chapter 2 - Basic principles of additive manufacturing: different additive manufacturing technologies." In *Additive Manufacturing*, edited by M. Manjaiah, K. Raghavendra, N. Balashanmugam and J. Paulo Davim, 17-35. Woodhead Publishing.

Leary, Martin. 2020. "Chapter 1 - Introduction to AM." In *Design for Additive Manufacturing*, edited by Martin Leary, 1-6. Elsevier.

Li, Hui, Yong Han, Weidong Shi, Taavi Tiganik, and Ling Zhou. 2022. "Automatic optimization of centrifugal pump based on adaptive single-objective algorithm and computational fluid dynamics." *Engineering Applications of Computational Fluid Mechanics* 16 (1): 2222-2242. https://doi.org/10.1080/19942060.2022.2143901. https://doi.org/10.1080/19942060.2022.2143901.

Lopes, João P., and Alírio E. Rodrigues. 2016. "Monolith reactors." In *Multiphase Catalytic Reactors*, 171-212.

Migliorini, Patrick J., Alexandrina Untaroiu, William C. Witt, Neal R. Morgan, and Houston G. Wood. 2014. "Hybrid Analysis of Gas Annular Seals With Energy Equation." *Journal of Tribology* 136 (3). https://doi.org/10.1115/1.4026590. https://doi.org/10.1115/1.4026590.

Moulijn, Jacob A., and Freek Kapteijn. 2013. "Monolithic reactors in catalysis: excellent control." *Current Opinion in Chemical Engineering* 2 (3): 346-353. https://doi.org/https://doi.org/10.1016/j.coche.2013.05.003. https://www.sciencedirect.com/science/article/pii/S221133981300052X.

Mr CFD. 2023. "Chemical Engineering." Accessed 26/04. https://www.mr-cfd.com/industries/chemical-engineering/.

Munson, B.R., B.G. Young, and T.H. Okiishi. 2005. *Fundamentals of Fluid Mechanics*. Wiley.

Ngo, Tuan D., Alireza Kashani, Gabriele Imbalzano, Kate T. Q. Nguyen, and David Hui. 2018. "Additive manufacturing (3D printing): A review of materials, methods, applications and challenges." *Composites Part B: Engineering* 143: 172-196. https://doi.org/https://doi.org/10.1016/j.compositesb.2018.02.012. https://www.sciencedirect.com/science/article/pii/S1359836817342944.

Önsan, Zeynep Ilsen, and Ahmet Kerim Avci. 2016. "Catalytic reactor types and their industrial significance." In *Multiphase Catalytic Reactors*, 1-16.

Pangarkar, Kalyani, Tilman J. Schildhauer, J. Ruud van Ommen, John Nijenhuis, Freek Kapteijn, and Jacob A. Moulijn. 2008. "Structured Packings for Multiphase Catalytic Reactors." *Industrial & Engineering Chemistry Research* 47 (10): 3720-3751. https://doi.org/10.1021/ie800067r. https://doi.org/10.1021/ie800067r.

Parra-Cabrera, Cesar, Clement Achille, Simon Kuhn, and Rob Ameloot. 2018. "3D printing in chemical engineering and catalytic technology: structured catalysts, mixers and reactors." *Chemical Society Reviews* 47 (1): 209-230. https://doi.org/10.1039/C7CS00631D. http://dx.doi.org/10.1039/C7CS00631D.

Quan, Haoyuan, Ting Zhang, Hang Xu, Shen Luo, Jun Nie, and Xiaoqun Zhu. 2020. "Photo-curing 3D printing technique and its challenges." *Bioactive Materials* 5 (1): 110-115. https://doi.org/https://doi.org/10.1016/j.bioactmat.2019.12.003. https://www.sciencedirect.com/science/article/pii/S2452199X19300714.

Raberger, Nikolaus, Michael Stutz, Nico Hotz, and D. Poulikakos. 2009. "Simulation of the Postcombustor for the Treatment of Toxic and Flammable Exhaust Gases of a Micro-Solid Oxide Fuel Cell." *Journal of Fuel Cell Science and Technology - J FUEL CELL SCI TECHNOL* 6. https://doi.org/10.1115/1.3080812.

Rapp, Bastian E. 2017. "Chapter 10 - Conservation of Mass: The Continuity Equation." In *Microfluidics: Modelling, Mechanics and Mathematics*, edited by Bastian E. Rapp, 265-271. Oxford: Elsevier.

Rehm, Bill, Drilling Consultant, Arash Haghshenas, Amir Saman Paknejad, and Jerome Schubert. 2008. "CHAPTER TWO - Situational Problems in MPD." In *Managed Pressure Drilling*, edited by Bill Rehm, Jerome Schubert, Arash Haghshenas, Amir Saman Paknejad and Jim Hughes, 39-80. Gulf Publishing Company.

SimScale. 2023. "What is CFD | Computational Fluid Dynamics?". Accessed 28/08/2023. https://www.simscale.com/docs/simwiki/cfd-computational-fluid-dynamics/what-is-cfd-computational-fluid-dynamics/.

Suvanjan, Bhattacharyya, P. Abraham John, Cheng Lijing, and Gorman John. 2021. "Introductory Chapter: A Brief History of and Introduction to Computational Fluid Dynamics." In *Applications of Computational Fluid Dynamics Simulation and Modeling*, edited by Bhattacharyya Suvanjan. Rijeka: IntechOpen.

Tu, Jiyuan, Guan Heng Yeoh, and Chaoqun Liu. 2013. *Computational Fluid Dynamics: A Practical Approach*: Elsevier/Butterworth-Heinemann.

Appendix A – Mesh Independence Tests

Mesh independence tests are used to prove that the solution obtained is invariant as the mesh is refined, i.e., as the mesh is refined with smaller elements, the computed solution should converge to a unique solution.

B.1. Method Validation

Table A.1. Values for the mesh independence tests for the validation geometry.

Element size / mm	Number of Elements	Average Velocity / $m \cdot s^{-1}$	Maximum Velocity / $m \cdot s^{-1}$	Average Pressure / Pa
2.5	807	1.9352×10^{-2}	2.630×10^{-2}	3.470×10^{-4}
2.0	1169	1.9378×10^{-2}	2.586×10^{-2}	3.734×10^{-4}
1.5	1663	1.9398×10^{-2}	2.808×10^{-2}	3.771×10^{-4}
1.0	3635	1.9444×10^{-2}	2.883×10^{-2}	3.791×10^{-4}
0.9	4231	1.9441×10^{-2}	2.833×10^{-2}	3.768×10^{-4}
0.8	5208	1.9450×10^{-2}	2.883×10^{-2}	3.767×10^{-4}
0.7	6867	1.9459×10^{-2}	2.895×10^{-2}	3.758×10^{-4}
0.6	9129	1.9465×10^{-2}	2.801×10^{-2}	3.742×10^{-4}
0.5	13248	1.9464×10^{-2}	2.908×10^{-2}	3.724×10^{-4}
0.4	20246	1.9468×10^{-2}	2.913×10^{-2}	3.708×10^{-4}
0.3	36167	1.9472×10^{-2}	2.916×10^{-2}	3.681×10^{-4}
0.2	80948	1.9474×10^{-2}	2.919×10^{-2}	3.654×10^{-4}

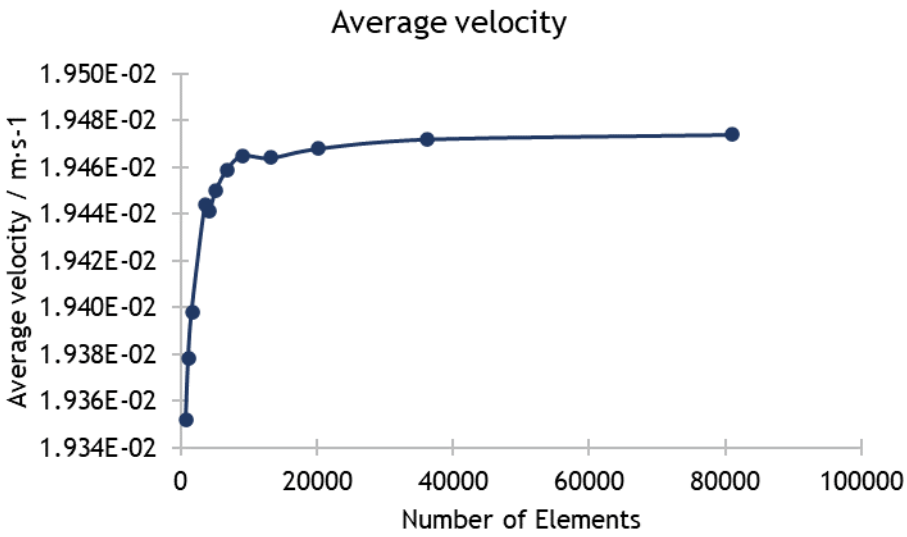

Figure A.1. Average velocity vs number of mesh elements.

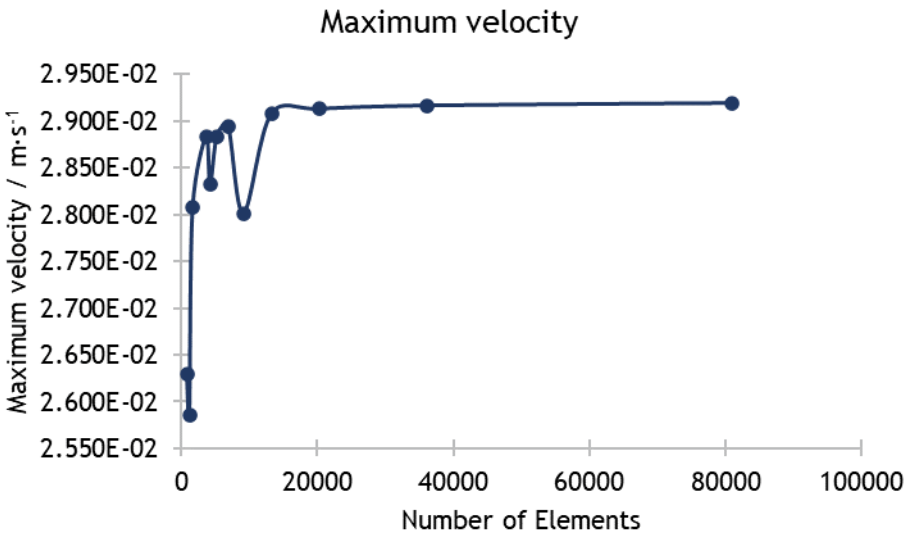

Figure A.2. Maximum velocity vs number of mesh elements.

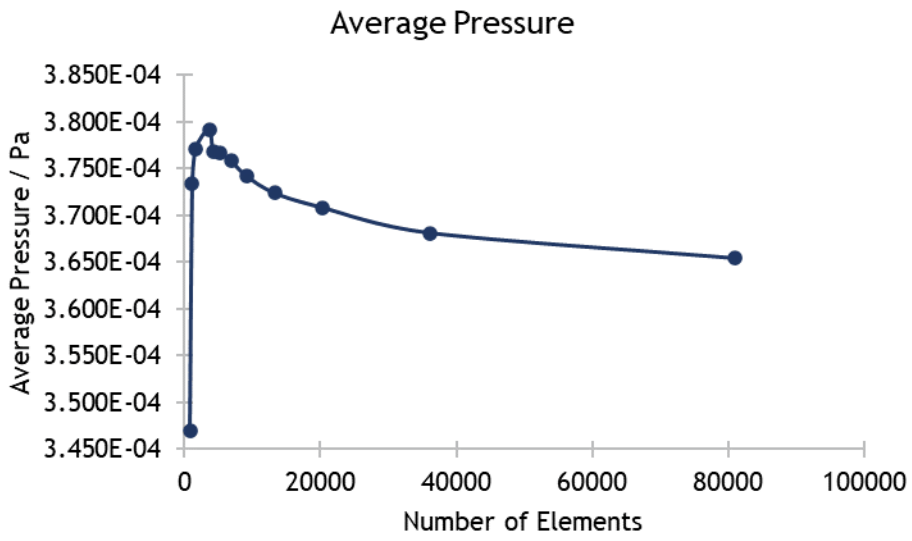

Figure A.3. Average pressure vs number of mesh elements.

Analysing these tests, it was possible to infer that the solution obtained is invariant for an element size of 0.4 mm (20246 elements).

B.2. Optimization

Table A.2. Values for the mesh independence tests for the optimization geometry.

Element size / mm	Number of Elements	Average Velocity / $m \cdot s^{-1}$	Average Pressure / Pa	Average mass fraction of H_2O
1.0	1151	0.1234	9.5524×10^{-3}	0.084607
0.9	1396	0.12517	9.7685×10^{-3}	0.084275
0.8	1819	0.12506	9.7223×10^{-3}	0.082663
0.7	2299	0.12637	9.8807×10^{-3}	0.083909
0.6	3073	0.12716	9.9446×10^{-3}	0.083621
0.5	4194	0.12825	1.0051×10^{-2}	0.083654
0.4	6795	0.12893	1.0086×10^{-2}	0.08314
0.3	11953	0.12948	1.0129×10^{-2}	0.083165
0.2	26419	0.12985	1.0138×10^{-2}	0.082438
0.1	10493	0.13006	1.0123×10^{-2}	0.082257

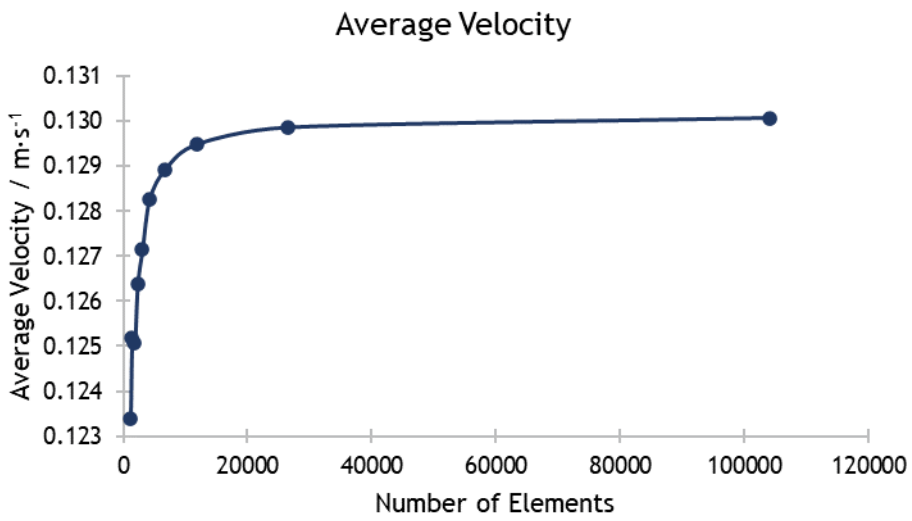

Figure A.4. Average velocity in the outlet vs number of mesh elements.

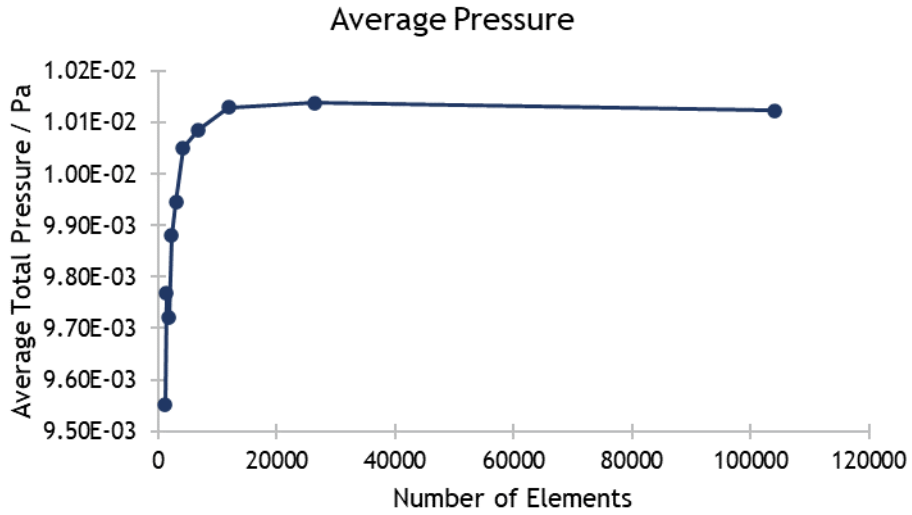

Figure A.5. Average Pressure at the outlet vs number of mesh elements.

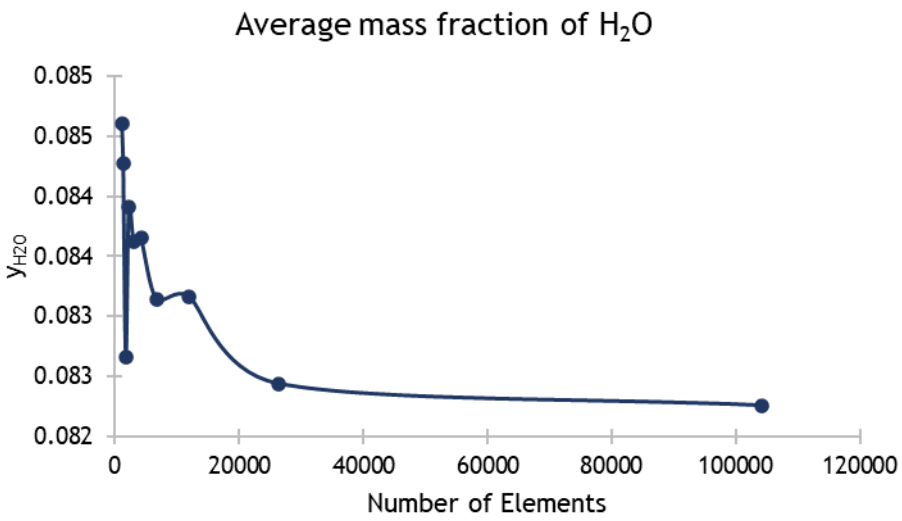

Figure A.6. Average mass fraction of H_2O vs number of elements.

Analysing these tests, it was possible to infer that the solution obtained is invariant for an element size of 0.2 mm (26419 elements).

Appendix B – Experimental Data

In this section, the experimental data collected for the various experimental runs are shown.

Table B.1. Measured volume and time for the calculation of the volumetric flow rates.

ω_{pump} / rpm	V / mL	t / s	Q / mL·s^{-1}	Q_{avg} / mL·s^{-1}	Q_{avg} / m^3·s^{-1}
30	10.0	16.75	0.597	0.568	5.68×10^{-7}
	20.0	35.75	0.559		
	20.1	36.2	0.555		
	20.0	35.61	0.562		
40	20.0	27.12	0.737	0.737	7.37×10^{-7}
	20.0	27.19	0.736		
	20.0	27.05	0.739		
50	20.0	21.19	0.939	0.943	9.43×10^{-7}
	20.0	21.23	0.942		
	20.0	20.98	0.953		
	20.0	21.32	0.938		

Table B.2. Residence time in the tubes for each test.

Rotational speed of the peristaltic pump / rpm	30	40	50
Residence time in the tubes / s	23.03	19.56	16.45

Appendix C – Hyperlinks to Animations and Experimental Videos

In this section, it is possible to access all the recorded videos of the experimental tests and the animations of the simulations (contours of mass fraction of tracer) by accessing the hyperlinks.

- Test A (30 rpm)
    - Experimental
    - Simulation
    - Comparison
- Test B (40 rpm)
    - Experimental
    - Simulation
    - Comparison
- Test C (50 rpm)
    - Experimental
    - Simulation
    - Comparison

Appendix D – History of Optimization Parameters

In this section, the histories of the different design parameters are shown, along with the upper and lower bound for the domain reductions.

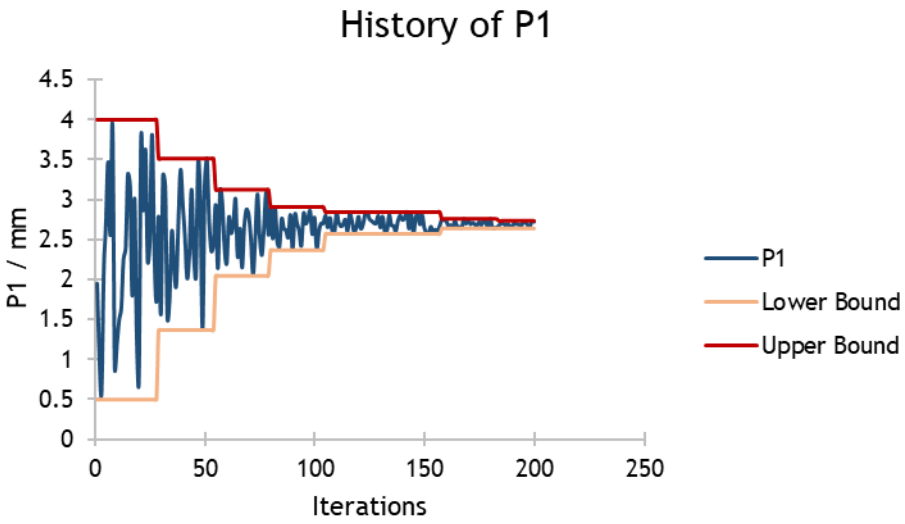

Figure D.1. History of P1.

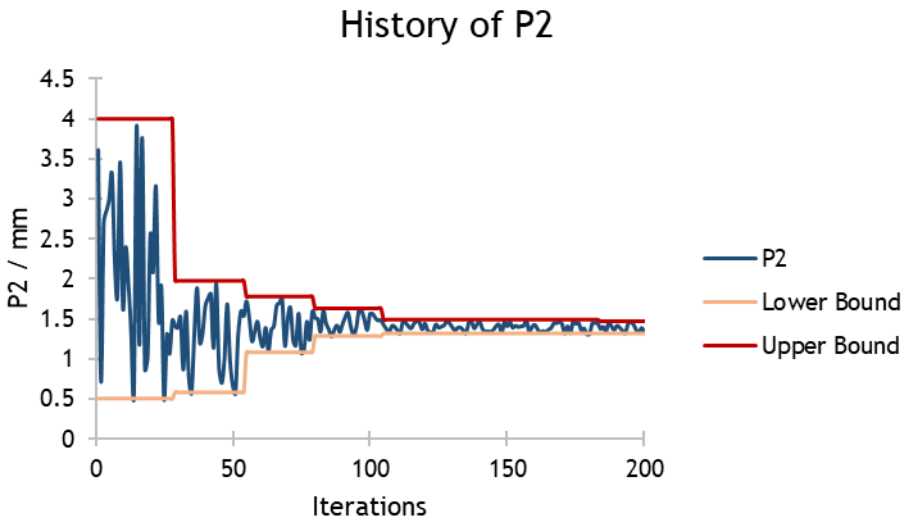

Figure D.2. History of P2

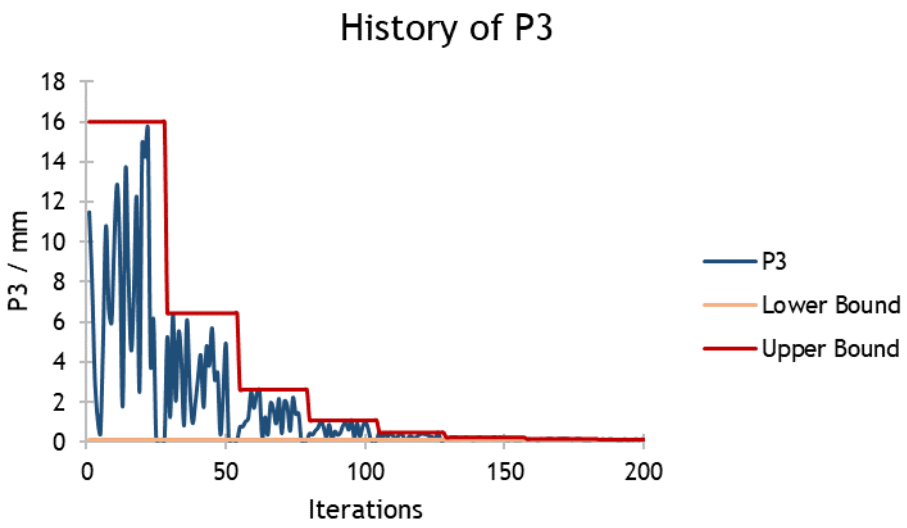

Figure D.3. History of P3.

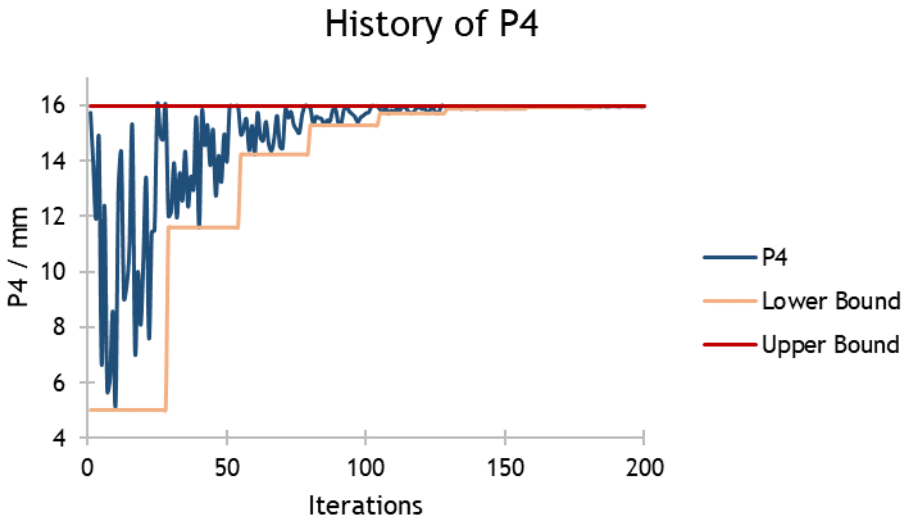

Figure D.4. History of P4.

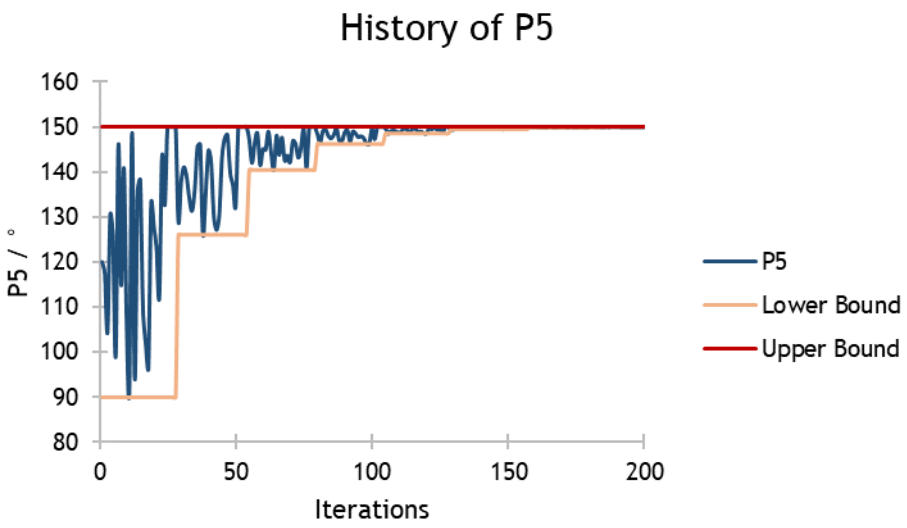

Figure D.5. History of P5.